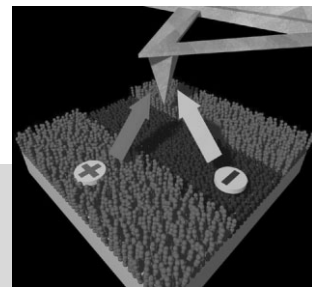


DOI: 10.1002/adma.200501394

Electronic Characterization of Organic Thin Films by Kelvin Probe Force Microscopy**

By Vincenzo Palermo, Matteo Palma,
and Paolo Samorì*



This review highlights the potential of Kelvin probe force microscopy (KPFM) beyond imaging to simultaneously study structural and electronic properties of functional surfaces and interfaces. This is of paramount importance since it is well established that a solid surface possesses different properties than the bulk material. The versatility of the technique allows one to carry out investigations in a non-invasive way for different environmental conditions and sample types with resolutions of a few nanometers and some millivolts. KPFM can be used to acquire a wide knowledge of the overall electronic and electrical behavior of a sample surface. Moreover, by KPFM it is possible to study complex electronic phenomena in supramolecular engineered systems and devices. The combination of such a methodology with external stimuli, e.g., light irradiation, opens new doors to the exploration of processes occurring in nature or in artificial complex architectures. Therefore, KPFM is an extremely powerful technique that permits the unraveling of electronic (dynamic) properties of materials, enabling the optimization of the design and performance of new devices based on organic-semiconductor nanoarchitectures.

[*] Dr. P. Samorì, Dr. V. Palermo
Istituto per la Sintesi Organica e la Fotoreattività
Consiglio Nazionale delle Ricerche
via Gobetti 101, I-40129 Bologna (Italy)
E-mail: samori@isof.cnr.it
Dr. P. Samorì, M. Palma
Nanochemistry Laboratory
Institut de Science et d'Ingénierie Supramoléculaires (I.S.I.S.)
Université Louis Pasteur
8, allée Gaspard Monge, F-67083 Strasbourg (France)

[**] We are grateful to our co-workers Drs. Andrea Liscio, Anna Maria Talarico, and Susanna Morelli for enlightening discussions. We also express our gratitude to long-term collaborators: Professors Klaus Müllen (Mainz), Roeland J. M. Nolte and Alan E. Rowan (Nijmegen), Franco Cacialli (London), and Giovanni Marletta (Catania). Financial supports from ESF-SONS-BIONICS, the EU through the NMP-STREP ForceTool, and the Marie Curie EST project SUPER, as well as from the bilateral program CNR-CNRS, are gratefully acknowledged. This article will also appear as a chapter in the upcoming book *Scanning Probe Microscopies Beyond Imaging: Manipulation of Molecules and Nanostructures* (Ed: P. Samorì), Wiley-VCH, Weinheim, Germany 2006.

1. Introduction

“Smart” organic molecules with tailor-made properties are promising materials for the fabrication of novel, cheap electronic devices such as flexible displays, chemical sensors, or large-area solar cells. Although a few of these devices have recently been introduced in the market, their work-up still needs to be optimized for large-scale applications.^[1] The performance of such devices can be improved by achieving full control over the supramolecular structure of the active organic components, and by unraveling and improving many other physico-chemical properties of such architectures, such as their complex electronic structure. These last peculiar properties make it somewhat difficult to explore these materials by means of conventional surface-sensitive techniques, such as photoelectron spectroscopy. Moreover, a very delicate problem in the context of electrical characterization of organic materials is the tailoring of a metallic/organic interface, i.e., the

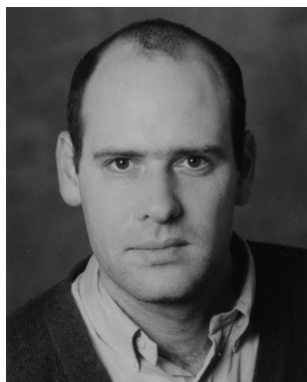
formation of a reliable ohmic contact, needed to electrically test the material under investigation. Therefore, non-conventional methodologies are required to study, in a non-invasive way, the structural and electrical properties of soft materials across a wide range of length scales.

Scanning force microscopy (SFM) allows the mapping of surfaces and interfaces with a resolution that spans from hundreds of micrometers down to the nanometer scale.^[2–4] The versatility of such methodology, which is also due to its applicability under different environmental conditions, makes it possible to gain insight into both the structural and dynamic properties of thin films. In this way, inorganic, organic, and biological materials can be studied, even in their native environments.

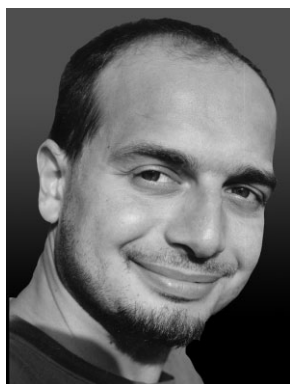
While surface-topography mapping by SFM is usually straightforward, the exploration of the chemical composition,

as well as the quantitative investigation of different physico-chemical properties, of the surface is more problematic.^[5] On the other hand, scanning tunneling microscopy (STM) and scanning tunneling spectroscopy (STS) techniques are very powerful methodologies which possess a chemical sensitivity and can achieve a subnanometer resolution.^[6,7] Nevertheless, their application is restricted to the first atomic layers of electrically conducting films. This, therefore, hinders their use for exploring working electronic devices, which are usually made up of thick conductive layers with alternating highly insulating areas.

Recently, a number of new SFM-based techniques exploiting electrically conducting probes have been developed.^[8] The primary physical properties they measure are current flows, resistance, capacitance, electrostatic forces, charge dis-



Paolo Samorì (Imola, Italy, 1971) obtained his Laurea in Industrial Chemistry at University of Bologna. He took his Ph.D. in Prof. J. P. Rabe's group (Humboldt University Berlin) on self-assembly of conjugated (macro)molecules at surfaces. After a postdoctoral position in the same lab, he was appointed in 2001 Researcher at the Institute for the Organic Synthesis and Photoreactivity of the National Research Council (ISOF-CNR), Italy. From 2003, he has been invited to hold a Visiting Professorship at the Institut de Science et d'Ingénierie Supramoléculaires of Université Louis Pasteur of Strasbourg (ISIS-ULP), France, where he is Director of the Nanochemistry Laboratory. His current research interests include the applications of scanning probe microscopies beyond imaging, self-assembly of hybrid architectures at surfaces, supramolecular electronics, and the fabrication of molecular-scale nanodevices. His work has been awarded various prizes, including the graduate student awards at EMRS (1998) and MRS (2000) as well as the IUPAC Prize for Young Chemists 2001.



Vincenzo Palermo (S. Severo, Italy, 1972) obtained his Laurea in Industrial Chemistry at the University of Bologna. He performed his Ph.D. at the Institute for the Organic Synthesis and Photoreactivity of the National Research Council (ISOF-CNR), Italy, working on characterization of silicon nanostructures for microelectronics. He worked in the groups of Prof. Y. K. Levine (University of Utrecht, The Netherlands) and Prof. R. A. Wolkow (National Research Council, Canada). He also worked in a joint project between ISOF-CNR and ST-Microelectronics for the nanoscopic characterization of silicon wafers. His current research interests include the morphological and electrical characterization of thin films for optoelectronics using scanning-probe techniques. His work has been awarded the graduate student award at EMRS (2003). He is presently a postdoctoral researcher at ISOF-CNR.



Matteo Palma (Roma, Italy, 1979) obtained his Laurea in Chemistry at the University of Rome, La Sapienza (Italy) with an experimental thesis on "Self-assembly and electrical properties of π -conjugated supramolecular architectures", performed under the supervision of Dr. Paolo Samorì at the ISOF-CNR, Bologna (Italy). In 2004, he started his Ph.D. in Dr. Paolo Samorì's group at the Institut de Science et d'Ingénierie Supramoléculaires of the Université Louis Pasteur of Strasbourg (ISIS-ULP), France, within the Marie Curie EST project "SUPER" (Supramolecular Devices at Surfaces). His current research is focused in particular on the development of prototypes of supramolecular wires at surfaces.

tribution, surface potential, and voltage drops on sub-100 nm length scales. These new SFM adaptations, i.e., conducting-probe SFM,^[9] scanning capacitance microscopy,^[10] electrostatic force microscopy,^[11] and Kelvin probe force microscopy,^[12] hold great promise for electronic characterization of materials since they allow simultaneous high-resolution topographic imaging as well as electrical and electronic characterization. In this review, we focus on the Kelvin probe force microscopy technique. Hitherto, this method has been labeled with different acronyms such as KPFM, KPM, SKPM, KFM, and SKM. For the sake of simplicity, we will hereafter utilize KPFM.

KPFM does not measure a current flow, but rather it records the electrostatic-force interaction between two objects, i.e., the tip and the sample. This measurement does not require a direct contact between the two objects;^[13] thus, KPFM is well suited for the study of fragile and soft samples such as organic materials. Further, its high voltage resolution, being about a few millivolts, allows the study of surface potential distributions or differences of a variety of thin films, including those possessing poor conductive properties.^[14] Being a non-contact and non-destructive method, it does not pose the risk of desorbing or removing even weakly bound species from the surface. In addition, it does not require particular sample treatments, such as exposure to high electric fields or electron or photon beams.

The Kelvin probe method is very versatile since, in contrast to other surface techniques, it can be employed to measure the work function of a wide range of materials under different experimental conditions over a wide range of temperatures, pressures, environments, etc.^[15] The work function (ϕ , see next section for a proper definition) is a very sensitive parameter which can provide evidence for micro- and nanoscopic structural and chemical variations, including the presence of contaminants. Moreover, unlike many other methods, measurement of ϕ by KPFM does not depend on an estimation of the electron-reflection coefficient on the surface.

Besides the use of KPFM since the early 1990s to study inorganic semiconductors and conventional Si-based devices

(see Sec. 5), a major effort has been recently applied to the exploitation of KPFM to characterize organic-semiconductor-based materials and devices.

This review offers an introduction to the KPFM technique. Due to the extremely large amount of work performed with this method in many scientific disciplines and on a variety of materials, encompassing metals, classical semiconductors, and organic and biological materials, this contribution will mainly address the use of KPFM on organic films and will not extensively cover all the obtained results. Particular emphasis will be given to the theoretical background of this method, to the qualitative and quantitative interpretation of the results with the highest possible resolution, and to the exploitation of this methodology to cast light onto the fundamental physico-chemical processes in working devices.

2. Kelvin Probe Scanning Force Microscopy

The Kelvin probe technique takes its name from William Thomson, also known as Lord Kelvin, who first introduced it in 1898^[16] to explain the formation of built-in contact potential differences in metals, which was previously observed by Alessandro Volta at the beginning of the 19th century.

To describe this phenomenon, the concept of work function (ϕ) has to be introduced. In its simplest definition, ϕ is the minimal energy needed to remove an electron from the electronic ground state in a given material. In a metal, ϕ can be described in terms of the free-electron model.^[17] It is usually defined as the difference in energy between an electron in the vacuum state and an electron at the Fermi energy of the metal (Fig. 1a). In other types of materials, such as semiconductors or insulators, it can be regarded as the difference in energy between the vacuum level and the most loosely bound electrons inside the solid.^[18]

When two plates of a capacitor composed of different materials are electrically wired together (Fig. 1b), electrons will flow from the material with the lower work function (weak electron binding, ϕ_2 in the figure) to the one with the higher

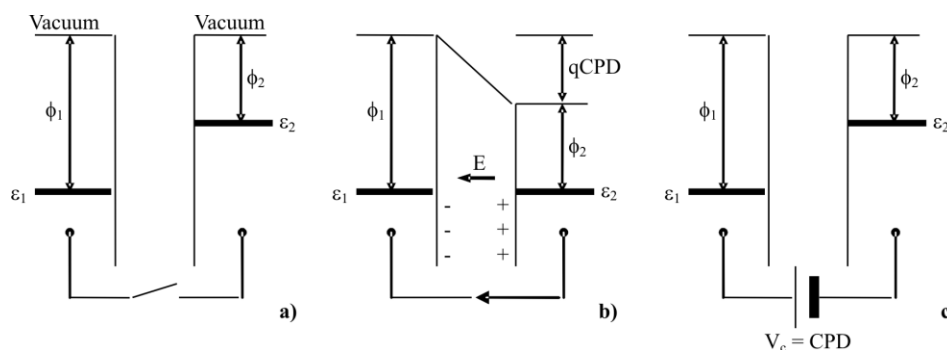


Figure 1. Schematic diagram of Kelvin Probe physics. a) Two materials 1 and 2 with different work functions ϕ_1 and ϕ_2 , corresponding to the energy difference between the Fermi level ϵ and the vacuum level. b) When the two materials are electrically contacted, electrons flow from 2 to 1 until the Fermi levels are aligned, leading to a contact potential V_b . The charges present in the two materials causes an electric field E . q : electron charge; CPD: contact potential difference. c) The electric field is removed by applying an external potential V_c which equals the contact potential.

work function (strong electron binding, ϕ_1 in Fig. 1), generating opposite charges on the capacitor plates and a contact potential difference (CPD) between the two materials. The presence of an electric field in the capacitor due to these charges can be then easily detected. An external potential V_c can indeed be applied to nullify this field. At equilibrium, the field is zero, and the externally applied potential equals the contact potential difference, which corresponds to the difference between the two work functions (Fig. 1c). Thus, if the work function of the reference plate (ϕ_1) is known, the work function of the material under study can be determined as $\phi_2 = \phi_1 - qV_c$, where q is the elementary charge.

Lord Kelvin realized this experimentally using a gold-leaf electroscope to measure the charge transfer upon electrical contact between two large, flat, polished discs of zinc and copper.

In 1932, Zisman improved the method by using a vibrating reference surface.^[19] In this vibrating capacitor setup, the mechanical oscillation, at frequency ω , induces changes in the system capacitance and thus in the reference plate voltage. This change in capacitance induces a small alternating current which can be easily detected. In fact, a periodic vibration of the distance between the two plates at ω results in a current $i(t)$ given by^[12]

$$i(t) = V_c \omega \Delta C \cos(\omega t) \quad (1)$$

where V_c is the contact potential difference and ΔC is the change in capacitance. For the actual measurement of the CPD, an additional voltage is applied between the two plates until the space in between becomes field-free and the current $i(t)$ goes to zero.

The classical Kelvin probe technique employing the Zisman concept has been used for macroscopic measurements of many materials by tracking shifts in the contact potential due to changes in the work function of the sample surface and to surface photovoltage effects.^[20,21] The attainable electrical resolution was very high, even down to ~ 1 mV. The major drawback was that the measured ϕ represented an average of the local work functions over the whole sample surface; thus, no detail on local ϕ variations on the sample surface could be achieved.

A few years after the advent of scanning force microscopy, Kelvin probe force microscopy was developed by Wickramasinghe and co-workers.^[12] In this setup, the reference capacitor plate is a sharp conductive SFM tip attached to a very flexible cantilever. The tip-sample interaction is highly localized, and potential differences between tip and sample can be detected by measuring the deflection of the cantilever due to electrostatic interactions, allowing measurement of ϕ with high spatial and electrical resolution.

In the Wickramasinghe KPFM setup,^[12] a conductive tip is scanned in non-contact mode^[3,4] on a sample surface, following its topography. The principle is similar to the Kelvin method, except that forces instead of currents are measured. An oscillating potential V_{ac} at frequency ω is applied to the tip during the scan. The tip interacts electrostatically with the surface, being attracted and repelled at the same frequency of

V_{ac} . Thus, an oscillation mode at a frequency ω appears on the cantilever. This oscillation is detected by the SFM photodiode, which sends a signal through a lock-in amplifier to isolate the oscillation mode at ω . The oscillation amplitude at frequency ω is proportional to the surface-potential difference between tip and surface. Nevertheless, this interaction could not be exactly quantified due to the complexity of the system dynamics and tip shape. Alternatively, qualitative two-dimensional (2D) maps of the surface potential can be obtained with the electrostatic force microscopy (EFM) technique.

In order to obtain an exact measurement of the work function of the sample, an additional feedback loop is added. This loop applies a given direct current (DC) offset potential voltage (V_{dc}) to the cantilever tip to minimize the electrostatic interaction between the tip and the surface (Fig. 2).

Both an alternating current (AC) and a DC voltage bias signal are then applied between the tip and the sample. In this case, the voltage between the tip and the sample can be expressed by

$$\Delta V = \Delta\phi - V_{dc} + V_{ac} \sin(\omega t) \quad (2)$$

where $\Delta\phi$ is the contact potential (difference in work function between the tip and the sample), V_{dc} is the DC offset potential applied to the tip, and V_{ac} and ω are the amplitude and frequency of the applied AC voltage signal, respectively.

Equation 2 can be used to derive an expression for the electrostatic force F between the tip and the sample, assuming a parallel-plate-capacitor geometry (other geometries can be also considered, although they require more complicated models).^[22] The energy U in a parallel plate capacitor can be expressed as

$$U = 1/2 C \Delta V^2 \quad (3)$$

where C is the local capacitance between the tip and the sample.

The force is then the rate of change of the energy with tip-sample separation distance, z

$$F = -\frac{\partial U}{\partial z} = -\frac{1}{2} \frac{\partial C}{\partial z} \Delta V^2 = F_{dc} + F_{\omega} + F_{2\omega} \quad (4)$$

with components at DC

$$F_{dc} = -\frac{1}{2} \frac{\partial C}{\partial z} \left[(\Delta\phi - V_{dc})^2 + \frac{V_{ac}^2}{2} \right] \quad (5)$$

and at frequencies ω and 2ω

$$F_{\omega} = -\frac{\partial C}{\partial z} [(\Delta\phi - V_{dc}) V_{ac} \sin(\omega t)] \quad (6)$$

$$F_{2\omega} = \frac{1}{4} \frac{\partial C}{\partial z} [V_{ac}^2 \cos(2\omega t)] \quad (7)$$

Information on the electrical properties of the sample can be obtained by isolating and then separately analyzing each of these three different force signals, i.e., F_{dc} , F_{ω} , and $F_{2\omega}$.

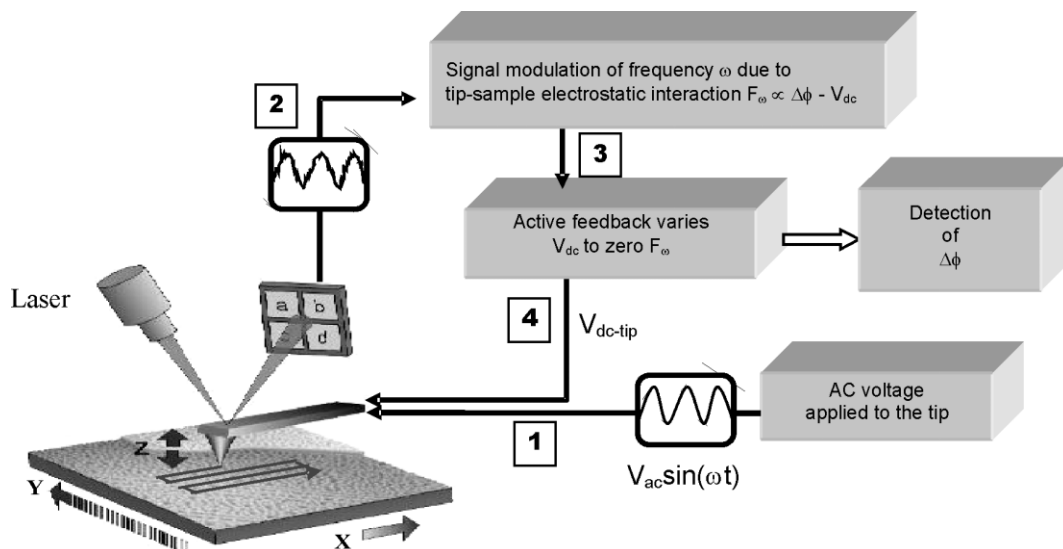


Figure 2. KPFM apparatus. 1) An alternating voltage V_{ac} is applied to the tip with a frequency ω . 2) The electrostatic tip–sample interaction induces a mechanical oscillation of the cantilever at a frequency ω . 3) The cantilever oscillation at ω is isolated using a lock-in amplifier and sent to a feedback circuit. 4) The feedback tries to minimize F_{ω} (which is proportional to the tip–sample interaction) by adding a V_{dc} voltage onto the tip. A different setup is in some cases exploited where the external potential bias is applied directly to the sample.

When the ω component of the electrostatic force interaction is zero, V_{dc} is equal to the difference in work function ($\Delta\phi$) between the tip and the sample surface ($V_{dc} = \Delta\phi$). Therefore, a 2D quantitative map of $\Delta\phi$ can be obtained by monitoring the voltage V_{dc} applied by the feedback signal. If the work function of the tip is known, the work function of the sample can be then determined. The ϕ of the tip can be easily obtained by calibrating the setup, making use of surfaces with known work functions. In essence, KPFM exploits the first harmonic component (F_{ω}) of the electrostatic-force interaction to determine the local work function on the sample surface.

Alternatively, as discussed in the next section, the measurements can be performed employing the frequency-modulation method (FM-KPFM), which uses the force gradient as a data-set instead of the force.

Furthermore, the 2ω component of the force on the tip can provide information on the local dielectric properties through the capacitance gradient $\partial C/\partial z$. This signal can be therefore used to gain insight into surface defects or heterogeneities.

Two different KPFM modes are commonly employed. In one, the Kelvin probe and the topographical signals are simultaneously detected at two different tip oscillation frequencies. In the other, a first scan collects the topographic signal while a second scan, performed at a larger tip–surface distance, records the Kelvin probe signal in the so-called “lift mode”.

3. Interpretation of the Signal in KPFM Measurements

The interpretation of images collected by KPFM is quite complicated and requires the use of theoretical models. To

correlate the effective surface potential distribution to the measured quantities, the KPFM setup can be modeled as a sample surface consisting of n ideally conducting electrodes of constant potential V_i and a tip of potential V_t .^[23] As demonstrated by Stemmer and co-workers, the measured KPFM potential does not exactly match the surface potential of a given location, but rather it is a weighted average of all the local potentials on the surface below the tip apex. The weighting factors of this average are the derivatives in z of probe-surface capacitances

$$V_{dc} = \frac{\sum_{i=1}^n (C'_{it} V_i)}{\sum_{i=1}^n (C'_{it})} \quad (8)$$

where V_{dc} is the voltage applied to the tip during the KPFM scan, V_i is the local surface potential at point i on the surface, and C'_{it} is the derivative of the capacitance versus distance between the tip and the point i on the surface.

It is worth noting that the first harmonic component of the tip force, F_{ω} , depends only on the mutual capacitances between tip and surface C_{it} and not on the mutual capacitances between different surface elements.

The surface is considered as an ensemble of capacitors plates of lateral dimensions Δx , Δy , and the V_{dc} measured by KPFM as a function of the capacitor location (x_i, y_i) can be expressed as^[23]

$$V_{dc}(x_i, y_i) = \int_{-\infty}^{+\infty} \int_{-\infty}^{+\infty} h(x - x_i, y - y_i) V(x, y) dx dy \quad (9)$$

$$h(x - x_i, y - y_i) = \lim_{\Delta x, \Delta y \rightarrow 0} \left[\frac{C'(x_i - x_t, y_i - y_t)}{C'_{tot} \Delta x, \Delta y} \right] \quad (10)$$

where C'_{tot} is the derivative of the total capacitance between tip and surface,

$$C'_{\text{tot}} \equiv \sum_{j=-\infty}^{+\infty} \sum_{i=-\infty}^{+\infty} C'(x_i - x_t, y_j - y_t) \quad (11)$$

and where x_t and y_t define the tip location. Equation 9 shows that the measured KPFM potential maps, i.e., $V_{\text{dc}}(x, y)$, are effectively 2D convolutions of the surface-potential distribution $V(x, y)$ with the corresponding transfer function $h(x, y)$ that is defined by the tip geometry.

Due to the long-range nature of electrostatic interactions, contributions to the KPFM signal always derive from the interaction of the surface with i) SFM tip apex, ii) the tip bulk, and even iii) the cantilever on which the tip is mounted. The cantilever contribution to the interaction is also relevant for a cantilever-sample distance of $\sim 15 \mu\text{m}$. Numerical simulations of KPFM on microscopic dots and sharp steps were performed to determine the influence of system geometry on KPFM resolution. Simple electrostatic calculations corroborated by experiments (Fig. 3) suggested that the effect of the cantilever dominates for tip-sample distances $z > 1000 \text{ nm}$, while it is very small for $z < 100 \text{ nm}$. As an example, Figure 3b shows the influence of tip-sample distance on the error in measuring the sample bias (i.e., V_{peak} or V_{valley}) for two purposely made metallic patterns.^[24] Moreover, it revealed that the highest resolution can be obtained using tips with a high aspect ratio, with a cantilever as small as possible and a relatively large tip apex (up to 100 nm).^[24,25]

More-refined calculations are difficult, since electrostatic forces and tip-sample capacitances depend both on the charge distribution as well as on the polarization of the tip and the

sample, and these in turn are affected simultaneously by the potential difference and by the tip-sample distance.^[26]

In addition, the tip does not lie at a constant distance from the surface, even when it follows, at best, the surface topography. This is due to the oscillation of the tip above the surface, as driven by the piezoactuator in the non-contact mode. Consequently, the tip-sample distance can vary continuously between 10 and 600 nm .^[27] The electrostatic interaction changes during the oscillation, and it reaches a maximum at the lower end of the tip swing. The effect of oscillation on the electrostatic force can be dominant if wide oscillations and tips having large masses are used.^[27]

Different methods have been employed to reduce the effect of long-distance interactions on KPFM measurements. While the conventional KPFM set-up uses amplitude modulation (AM) to detect the electrostatic force F , a possibility to experimentally reduce long-range electrostatic contributions is to measure instead the force gradient along the z axis: $\nabla = \partial F / \partial z$.

The forces due to the interaction of the sample with both the cantilever and the cone of the tip vary only slowly in proximity of the sample compared to the tip's apex-sample interaction; therefore, they can be separated. This is only correct when the oscillation amplitude of the tip is small compared to the range over which the potential varies significantly.^[28]

To measure the force gradient, one can use the frequency shift^[26] or phase shift^[28–30] of the tip oscillation at ω . The corresponding techniques have been called FM-KPFM and EFM-phase, respectively.

In these measurements, the tip is oscillated during the lift scan as described in Section 2: the tip's resonant frequency and phase shift due to the electrostatic-force gradient $\partial F / \partial z$

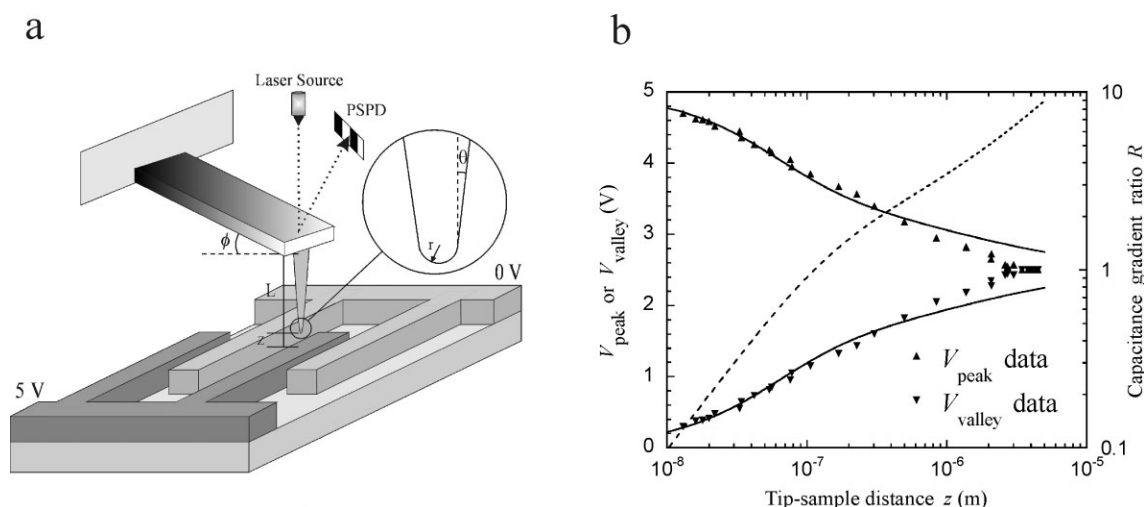


Figure 3. a) Schematic diagram of the scanning probe and the test structure used in [24] to study the influence of tip-sample distance z on the measured potential. The test structure consists of alternating electrodes coming out from each of two macroscopic metal pads, which were biased to 0 and 5 V. The width of the electrodes, as well as the spacing between them, is $1.7 \mu\text{m}$. The tip is modeled as a hemisphere at the end of a truncated-conical part (shown magnified in the inset). PSPD: photosensitive position detector. b) Experimentally observed variations with z of V_{peak} (voltage measured over 5 V biased finger, shown as triangles) and V_{valley} (voltage measured over 0 V biased tip, shown as inverted triangles) are compared to theoretically calculated variations (shown by two dark lines, upper one for V_{peak} and lower one for V_{valley}). The calculated ratio of the capacitance gradient of the cantilever to that of the tip, R , plotted against z is also shown by a dashed line. Reprinted with permission from [24]. Copyright 2001 American Institute of Physics.

are probed. For small force gradients, the resonant frequency shift and phase shift are^[29]

$$\Delta\omega = \frac{\omega_0}{2k} \frac{\partial F}{\partial z} \quad (12)$$

and

$$\Delta\phi = \arcsin\left(\frac{Q}{k} \frac{\partial F}{\partial z}\right) \quad (13)$$

where ω_0 is the resonant frequency, k is the spring constant, and Q is the quality factor of the cantilever. Since for a parallel plate capacitor

$$\frac{\partial F}{\partial z} = -\frac{1}{2} \frac{\partial^2 C}{\partial z^2} (\Delta V)^2 \quad (14)$$

by combining Equations 12, 13, and 14 the frequency and phase shift can be directly related to the potential difference ΔV

$$\Delta\omega = -\frac{\omega_0}{4k} \frac{\partial^2 C}{\partial z^2} (\Delta V)^2 \quad (15)$$

$$\Delta\phi = -\arcsin\left(\frac{Q}{2k} \frac{\partial^2 C}{\partial z^2} (\Delta V)^2\right) \quad (16)$$

This means that the phase and frequency shift are squared functions of the potential difference ΔV between the tip and the sample, and that the resolution of the technique is determined by the lateral variations of the gradient $\partial^2 C/\partial z^2$. The phase shift is always negative, because $\partial^2 C/\partial z^2$ is positive.^[29]

A simple analytical model describing tip–surface interactions has been also reported.^[25,31] A very precise estimation of $\partial C/\partial z$ components of the electrostatic interaction can be achieved by modeling the tip as a hemisphere and a truncated cone in the study of relatively simple structures (spherical Au- or CdSe-based nanoparticles). The use of simple and regular structures, such as well-defined silicon dots, even allows the determination by KPFM of the amount of charge present in a structure, down to single electrons.^[25,31]

A detailed experimental and theoretical study of the accuracy and resolution provided by the amplitude-sensitive method and the frequency-modulation method has been recently reported.^[32] Comparing the two approaches, Zerweck and co-workers clearly proved that the frequency-modulation method is preferable in most applications because it provides much higher lateral resolution, yields quantitative surface potential values on areas larger than the tip radius, and is not significantly affected by variations of the tip–sample distance during topographic imaging.^[32]

When the Kelvin probe and the topography measurements are performed simultaneously without using a second scan (i.e., lift mode), an inversion in the image contrast can occur, i.e., some areas seem to have a lower potential compared with the background while it seems higher in others, even when recording a single image. This is due to the contribution of non-electrostatic forces to the V_{dc} KPFM signal.^[33] In order to efficiently separate the electrostatic force signal from the non-

electrostatic forces signal, the amplitude of the AC bias in the FM-mode KPFM must be relatively large.^[33]

KPFM measurements can be performed in a different way by applying the bias voltage $V(t) = |V_{dc}| + V_{ac} \sin(\omega t)$ directly to the sample, holding the tip at ground potential. However, an influence of the AC sample voltage on the measured contact potential has to be taken into account. This dependence can be explained by bias-induced band bending at the semiconductor surface.^[34]

4. Electronic Characterization of Organic Semiconductors

In a semiconductor, the combination of atomic orbitals leads to the formation of a conduction and a valence band, with a well-defined forbidden energy gap in the middle. Electrons are free to move throughout the solid in the extended electronic bands. This allows reaching a thermal equilibrium, leading to Fermi-level alignment and band-bending phenomena in the case of a metal/semiconductor contact. This can be described with the well-known Mott–Schottky model (Fig. 4b).^[35]

Although the organic materials applied as active components in electronic devices are usually called organic semiconductors, their highest occupied molecular orbital–lowest unoccupied molecular orbital (HOMO–LUMO) gap is typically quite large, i.e., 2–3 eV. The concentration of thermally excited carriers is thus extremely small, like that of an insulator. Consequently, the formation of valence and conduction bands, thermal equilibrium, and thus Fermi-level alignment and band bending at the interfaces cannot be assumed a priori since the HOMO–LUMO separation is usually much larger than the thermal energy. Notably, an interfacial dipole cannot be neglected for most organic/metal interfaces as the potential shift at the interface due to such dipoles sometimes reaches over 1 eV, in contrast to the assumption of the common vacuum level in the Mott–Schottky model (Fig. 4c).^[36,37]

Furthermore, the conventional techniques applied for band-bending measurements, such as ultraviolet photoelectron spectroscopy (UPS) or X-ray photoelectron spectroscopy (XPS), cannot always be employed because of the high resistance of the organic materials, which leads to sample charging during the measurement. In contrast, Kelvin probe microscopy provides insight into band bending, even with materials with poor electrical properties.^[38]

In the case of an organic/metal interface, if the total number of the available mobile carriers in the organic film is sufficiently large, there will be a charge redistribution nearby the interface within the reasonably short time of an experiment.^[39] In the case of Figure 4a, for example, the work function of the metal is larger than that of the organic layer, and the electrons prefer to reside in the metal. As a result, some electrons may move from the organic layer to the metal, leading to negative and positive charging of the metal and the organic layer, respectively. This charging decreases the affinity of the metal for the negatively charged electrons.

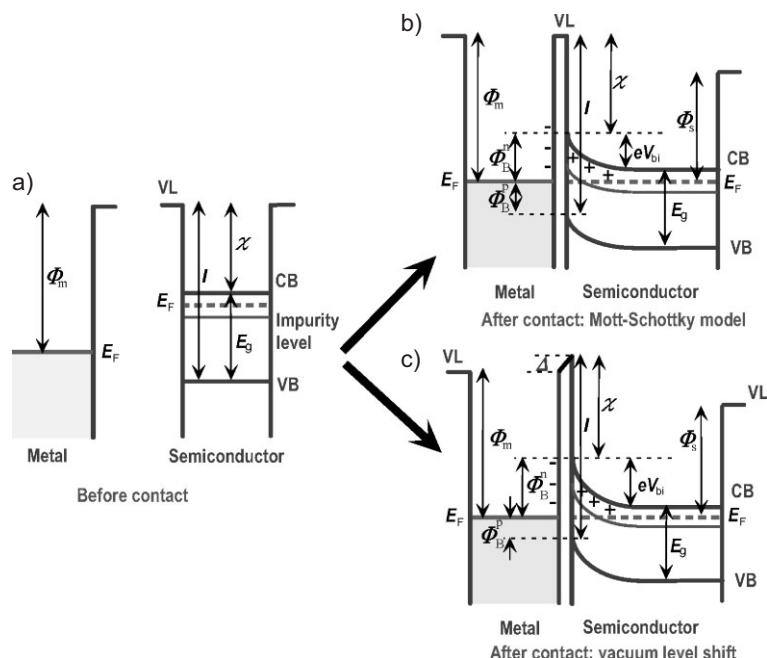


Figure 4. Models for energy-level alignment at organic semiconductor/metal contact: a) Energy diagram before contact. b) Mott-Schottky model assuming vacuum-level alignment at the interface and band bending with Fermi-level alignment. c) Realistic model including vacuum level shift at the interface. The barrier height for hole injection is $\phi_B^p = I - \phi_m^p$ for a p-type semiconductor, while for a n-type semiconductor it is $\phi_B^n = \phi_m^n - \chi$. In the image, VL, CB, VB, E_F and E_g are the energy levels of the vacuum, conduction, and valence bands, the Fermi level, and the energy gap, respectively. ϕ_m , ϕ_s , ϕ_{bi} , and V_{bi} are the work functions of metal and semiconductor, the barrier height for n and p charge injection, and the built-in junction voltage. I and χ are the ionization energy and the electron affinity of the solid, respectively, and Δ is the surface dipole. Reprinted from [37].

This flow and distribution of charge continues until the Fermi levels of the metal and that of the bulk of the organic layer are aligned. In such a redistribution of charges, the potential distribution at the interfacial region can be described by the Poisson equation, which expresses the relation between the charge and potential distributions. As a result, a diffusion layer (also known as depletion layer) with band bending is formed, characterized by a built-in potential V_{bi} in the organic film.^[35,40,41] The thickness of the diffusion layer w depends on factors such as V_{bi} , the dielectric constant of the organic layer ϵ_r , and the spatial distribution of the available donor or acceptor levels.^[39] In organic devices, band bending is closely related to the potential profile across the organic layer when an external electric field is applied, which promotes the redistribution of charges. Nevertheless, for a very thin layer of molecular material, a nearly flat band in the interfacial region are expected.^[39]

For metal/organic junctions, a dipole layer may be formed directly at the interface due to various origins, such as charge transfer across the interface, redistribution of the electron cloud, interfacial chemical reactions, and other types of electronic-charge rearrangement.^[42,43] Such interfacial-dipole formation will originate an abrupt shift of the potential

across the dipole layer^[44] leading to a shift of the vacuum level (ΔVL) at the interface, as shown in Figure 4c. The value of Δ is determined by the magnitude of the dipole. This leads to the shift in VL in the organic layer on the right-hand side in Figure 4 from that of the metal on the left-hand side. While Nielsen pointed out the importance of such interfacial dipole layers in 1974,^[44] the experimental contributions to gain insight into such an issue have been very scarce. Consequently, this factor has often been neglected in the field of organic devices. On the other hand, this possible shift of the VLs is well known in the field of surface science.^[42,43] It is usually referred to as the change in the work function (or surface potential) of the metal.^[43] To better understand the origin of surface-dipole-induced shifts of the vacuum level, it is indeed worth pointing out that the concept of a vacuum level is not at all straightforward.^[39]

Usually, the vacuum level is defined as the energy of an electron at rest at an infinite distance from the sample, $VL(\infty)$, but for most measurements of electron affinity, ionization potential, and work function, the reference vacuum level is the energy of an electron just outside the sample, at a short distance from the surface, where the role played by the potential of the solid is not negligible.^[42,45] The effect of the solid on this vacuum level at the surface ($VL(s)$) is most convincingly demonstrated by the well-known dependence of the work function on the surface of a single crystal. Since the Fermi level is a common level inside the solid, this dependence is due to the energy difference of an electron just outside of the solid, as shown in Figure 5.

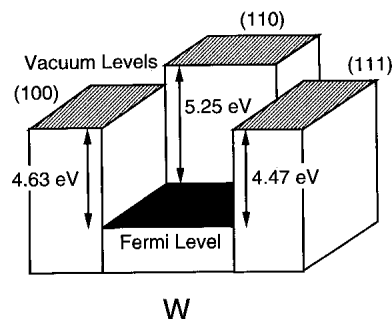


Figure 5. Dependence of the work function of a tungsten single crystal on the crystalline surface considered. The energy of the vacuum level at the surface, i.e., $VL(s)$, is different for the (100), (110), and (111) surfaces. Reprinted from [39].

As the distance from the surface becomes larger, the energy of the free electrons gradually converges to a common value, which corresponds to what we called $VL(\infty)$. For a metal, the

difference between the energies of $VL(\infty)$ and $VL(s)$ is mostly due to the surface dipole layer formed by the tailing of the electron cloud at the surface. For organic solids, the existence of a surface dipole layer comparable to that of a metal surface has not yet been thoroughly experimentally investigated. For the case of solids consisting of non-polar molecules, one can expect a relatively small surface dipole.^[39]

Interestingly, Seki et al. studied the work function of various metals, such as Ca, Mg, Cu, Ag, and Au, when coated with a typical hole-injection layer, such as *N,N'*-bis(3-methyl-phenyl)-*N,N'*-diphenyl-[1,1'-biphenyl]-4,4'-diamine (TPD).^[46] The work function's change was analyzed using the Kelvin probe method and UPS up to a film thickness of 100 nm. The results showed that band bending leading to Fermi-level alignment is not achieved, at least for systems prepared and measured under ultrahigh vacuum conditions.

Comparative studies of band bending in organic materials have been carried out on C_{60} fullerene, TPD, and tris(8-hydroxyquinoline)aluminum(III) (Alq_3) thin films.^[37] Gradual band bending was observed for C_{60} /metal interfaces revealing a width of the space charge layer of about 100 nm. On the other hand, a flat band feature was detected for TPD/metal interfaces, probably because of its high purity. These results demonstrate that the model of band bending used in inorganic-semiconductor interfaces is still valid for organic semiconductors, although much thicker films are often necessary to achieve bulk Fermi-level alignment. For Alq_3 /metal interfaces, a new type of band bending was observed where the energy levels changed as a linear function of the distance from the interface.^[37]

In inorganic semiconductors, the surface states typically lie in the forbidden gap and can pin the Fermi level at the surface, hindering band bending. For organic semiconductors, the surface states are usually outside the optical gap, and thus surface-states pinning is less common.^[38] Furthermore, even surface states associated with dangling bonds present at cleaved surfaces of inorganic semiconductors typically pin the Fermi level and hinder any electrostatic measurement of the band structure in the bulk. These surface charges are generally absent in van der Waals'-bonded organic materials, making KPFM particularly suitable for organic compounds.^[47]

It is important to point out that very often the KPFM method can also be employed to explore thin, almost insulating

organic films. When a null charge condition is achieved, the electric field E in the capacitor gap is zero, and the vacuum level of the reference electrode coincides with the vacuum level of the sample, even though charges may be induced both in the layer and at the surface region of the substrate on which the sample film is formed. Thus, the KPFM method correctly maps the surface-potential distribution even when the sample is poorly conducting.^[37,38]

5. KPFM of Conventional Inorganic Materials

KPFM measurements of the contact-potential difference between different materials were performed for the first time by Wickramasinghe and co-workers.^[12] The possibility of simultaneous topographical and electronic characterization on the nanometer scale was in this way demonstrated. In this set of experiments, several images of different metals such as gold, platinum, and palladium were taken in order to demonstrate the performance and reliability of the new technique. These measurements were carried out in air using either gold-coated silicon or nickel/chrome tips (Fig. 6).

KPFM also allowed the detection of surface contamination of metallic surfaces with carbon-based materials by tracking the ϕ value.^[48]

KPFM investigations have subsequently been extended to conventional semiconductors such as silicon.^[49] Dopant-concentration profiles in two dimensions were studied at size scales below 100 nm. Such results were obtained using gold-coated and uncoated silicon tips, setting the V_{ac} frequency ω at one of the resonance frequencies of the cantilever. The measurements were stable and reproducible, albeit the quantitative determination of dopant concentration was not achieved. The error due to surface-oxide charges present on the semiconductor surface was estimated to be below 50 mV.^[49]

In addition KPFM, in combination with scanning capacitance microscopy (SCM), has been employed to detect the surface-potential changes in a silicon p-n junction. In this combined measurement, KPFM has been used to map surface potential distributions while SCM allowed the mapping of the charge-carrier density (Fig. 7). Surface-potential differences between the KPFM results and theoretical expectations were

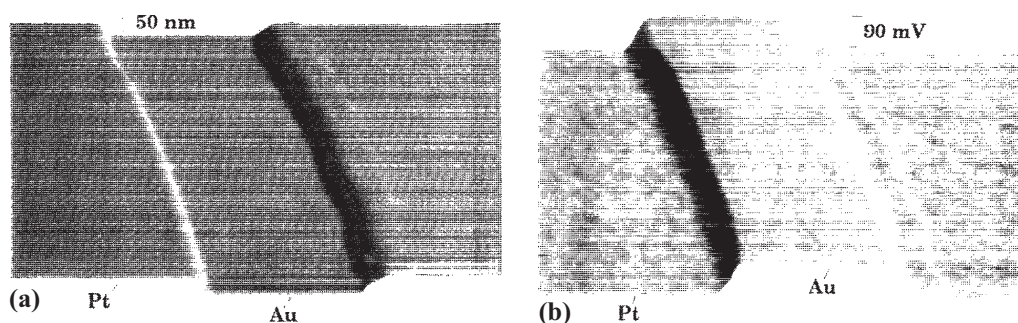


Figure 6. Comparison of topographic and CPD image ($8\ \mu\text{m} \times 6\ \mu\text{m}$) of platinum on gold. Reprinted with permission from [12]. Copyright 1991 American Institute of Physics.

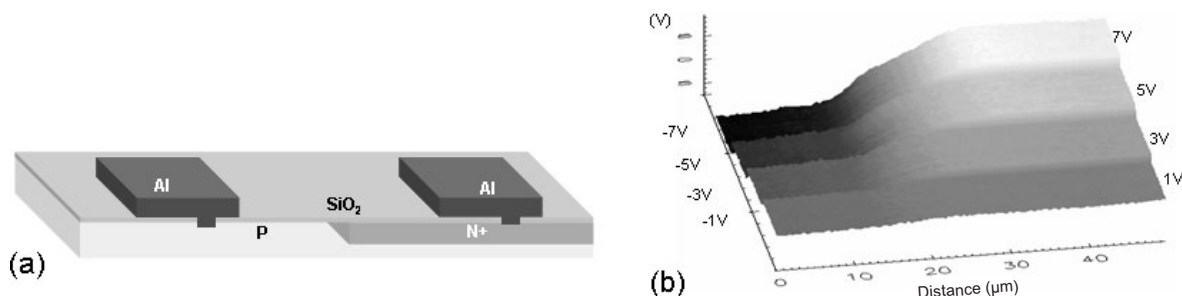


Figure 7. a) Schematic diagram of a model p–n junction diode with Al contacts. b) Three-dimensional potential profiles measured with KPFM under various reverse-bias conditions (1 V for n-type and –1 V for p-type, 3 V for n-type and –3 V for p-type, 5 V for n-type and –5 V for p-type, and 7 V for n-type and –7 V for p-type). Reprinted with permission from [50]. Copyright 2000 American Institute of Physics.

ascribed to the presence of oxide charges with a density of $\sim 10^{11} \text{ cm}^{-2}$.^[50] Surface-state pinning did not prevent KPFM measurements on p–n junctions, while the removal of adsorbed water improved the resolution.^[51]

Another very interesting application of KPFM has been the measurement of minority-carrier diffusion length in conventional semiconductors.^[52,53] The method is based on the study of the surface photoinduced voltage between the SFM tip and the surface of an illuminated semiconductor p–n junction. The photogenerated carriers diffuse to the junction and change the voltage difference between the tip and the sample as a function of the horizontal distance from the p–n junction. The diffusion length L is then obtained by fitting the measured contact-potential difference using the minority-carrier continuity equation. The method was applied to determine the electron diffusion length in GaP p–n and Schottky junctions (Fig. 8).^[53]

KPFM measurements have also been performed on quantum dots,^[54,55] quantum wells under illumination,^[56] laser diodes,^[57] nanotubes,^[58,59] and chemically sensitive field-effect transistors.^[60] This technique permitted the measurement of

the size dependence of the work function for different nanostructures, such as multi-walled nanotubes,^[61] and the charging behavior of dots.^[55] One of the most promising applications of KPFM is indeed its use on working devices, where the effect of current or light passing through the device can be observed on different areas of the device. Jiang et al. used KPFM to observe the effect of illumination on charge generation and potential build-up on solar cells, performing the measurements jointly with macroscopic current–voltage and cyclic voltammetry characterizations.^[62,63] KPFM investigations on solar cells which contained single and multiple layers of Cu(In,Ga)Se₂ and GaInP₂ showed a complex distribution of built-in electrical potential. In multicomponent solar cells, selective charging of one of the different layers composing the cell can be obtained using light of different wavelengths. In this direction, KPFM has been recently used with a higher resolution to study the fine structure of Cu(In,Ga)Se₂ solar cells^[64,65] and CuGaSe₂ solar cells,^[66] observing the effect of grain boundaries on charge generation and collection. It has been shown that KPFM allows the observation of positively charged grain boundaries which are not visible in the topogra-

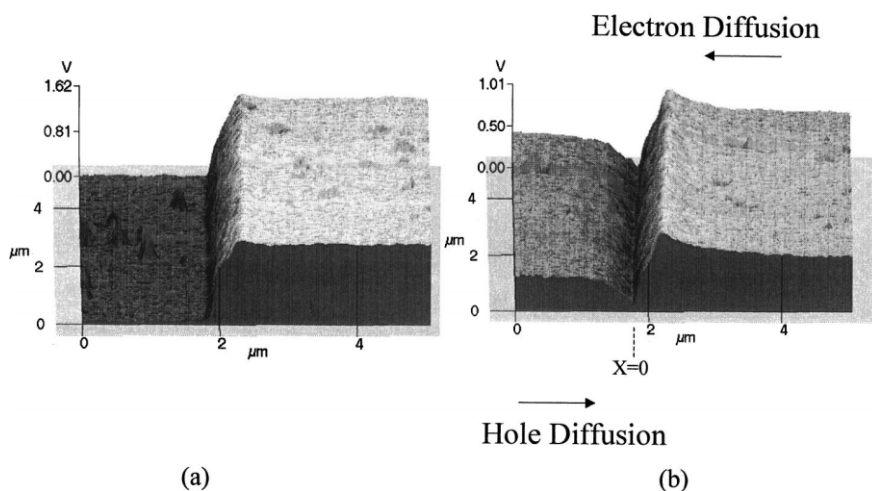


Figure 8. Two-dimensional potential difference images of the cleaved GaP p–n junction a) in the dark and b) under super-bandgap ($\lambda = 488 \text{ nm}$) illumination. The minority-carrier diffusion on both sides of the p–n junction can be clearly observed in (b). Reprinted with permission from [53]. Copyright 2000 American Physical Society.

phy, and the identification of the locations where the potential is lower than in the grain bulk.^[64,65] By correlating the KPFM results with macroscopic measurements of photocurrents, it was possible to identify the cell composition giving the best device performance.

6. KPFM on Organic Monolayers, Supramolecular Systems, and Biological Molecules

KPFM explorations have been performed on a wide variety of ordered molecular architectures, such as self-assembled monolayers (SAMs), Langmuir–Blodgett (LB) films, and even single molecules, with high lateral and voltage resolutions.

A classical SAM is formed from solution by chemisorption of crystalline alkanethiols monolayers onto a metallic surface, e.g., a Au(111) crystal. The versatility of such a method allows the formation of a variety of different monolayers with diverse chemical compositions and orientations.^[67–69] KPFM has been employed to explore the electronic properties of phase-separated SAMs of different alkanethiols on Au(111). This study revealed a dependence of the CPD on the molecular length. The measured CPD was found to increase linearly by either 9 mV (Fig. 9)^[70] or 14 mV^[71] per CH₂ unit. This result was ascribed to the changing dielectric behavior of the hydrocarbon-tail region.

In SAMs of aromatic oligomers bearing a thiol end group, the molecular dipole is typically oriented downwards, i.e., towards the surface. Due to this reason, a negative change in the surface potential distribution between the uncovered and the SAM-covered gold was observed.^[72] For aromatic molecules, the delocalization of the electron cloud is higher than in alkanethiols, and thus the decrease in surface potential, proportional to the molecule length, saturates and reaches a fixed value already when three aromatic rings are attached to gold.

The surface potential difference between two different SAMs can be calculated with a good approximation from the molecular dipoles of different molecules (Fig. 10)^[73]

$$\Delta V_{\text{SAM1-SAM2}} = \frac{\left[\frac{\mu_{\text{SAM1}}}{(\epsilon_{\text{SAM1}} A_{\text{SAM1}})} - \frac{\mu_{\text{SAM2}}}{(\epsilon_{\text{SAM2}} A_{\text{SAM2}})} \right]}{\epsilon_0} \quad (17)$$

$$\mu = \frac{\mu_0}{(1 + 9an^{3/2})} \quad (18)$$

where μ is the actual molecular-dipole moment normal to the substrate, μ_0 is the molecular-dipole moment in the absence of depolarizing effects, A is the area occupied by each molecule, ϵ is the dielectric constant, ϵ_0 is the permittivity of free space, a is the polarizability of a molecule, and n is the number of dipoles per unit area.

Using ab-initio calculations, the relationship between surface voltage, dipole moment, and work function has been de-

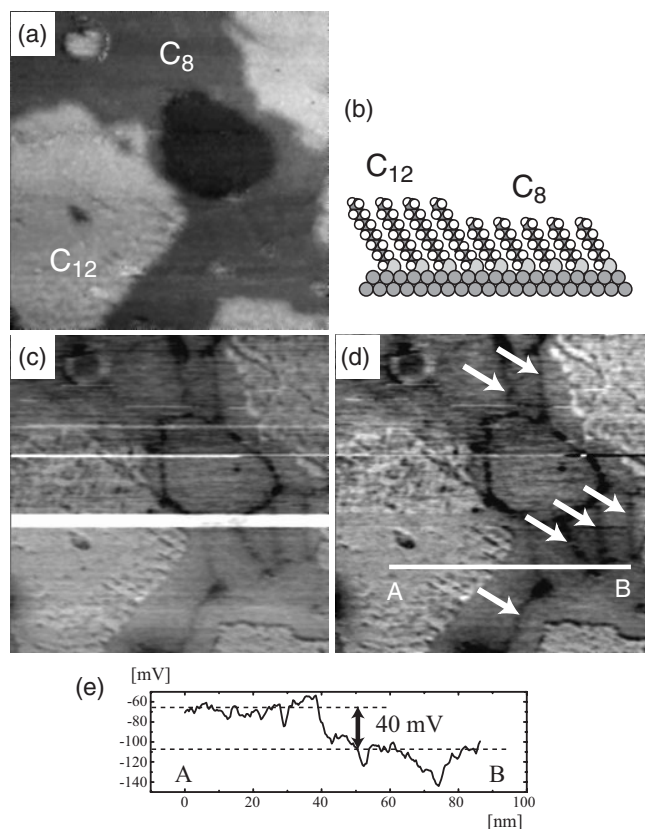


Figure 9. a) Non-contact SFM image of a C₈/C₁₂ phase-separated SAM (100 nm × 100 nm). b) Schematic illustration of possible structure models of the C₈/C₁₂ phase-separated SAM. c) Surface-potential image obtained simultaneously with (a). d) Filtered surface-potential image reduced the effect of “tip changes” from (c); narrow regions with lower surface potential (indicated by arrows) can be seen in the C₈ domains: these regions probably correspond to the domain boundaries of the C₈ domains which are barely seen in the topographic image. e) Cross-sectional plots taken on the unfiltered surface-potential image. Reprinted with permission from [70]. Copyright 2004 Institute of Physics.

termined for SAMs with different chemical compositions supported on silicon (Figs. 10,11) as

$$\Delta V_{\text{SAM1-SAM2}} = \frac{\phi_{\text{SAM1}} - \phi_{\text{SAM2}}}{e} \quad (19)$$

where e is the electron charge.

The comparison between calculated and measured surface potentials allowed the determination of the molecules’ surface densities for the different layers (Fig. 11). The measured differences in surface potential were related to the different energies and geometries of the HOMO and LUMO for each molecule (Fig. 12).

SFM and KPFM experiments on LB films of modified hexa-*peri*-hexabenzocoronenes (HBCs) allowed measurement of the effect of the molecular order on the electronic struc-

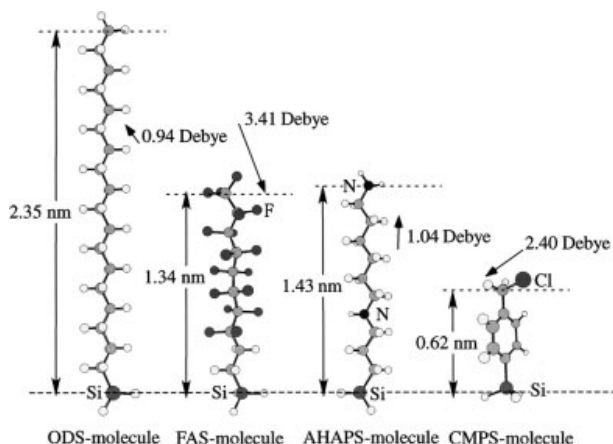


Figure 10. Molecular structures and dipole moments for different molecular systems. From left to right: *n*-octadecyltrimethoxysilane (ODS), heptadecafluoro-1,1,2,2-tetrahydro-decyl-1-trimethoxysilane (FAS), *n*-(6-aminohexyl) aminopropyltrimethoxysilane (AHAPS), and 4-(chloromethyl) phenyltrimethoxysilane (CMPS). Reprinted from [73].

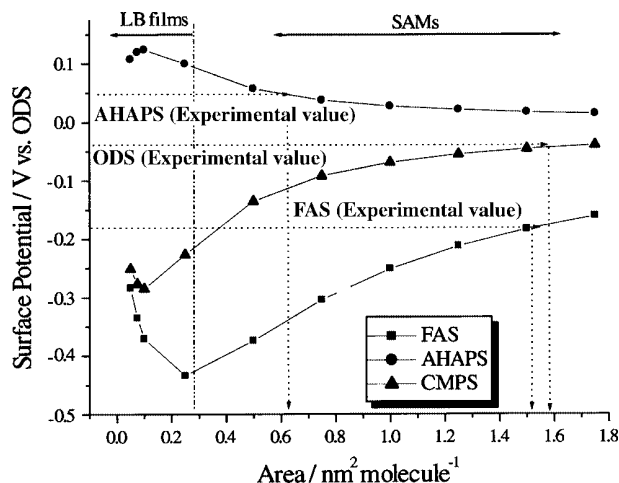


Figure 11. Calculated surface potentials for FAS-, AHAPS-, and CMPS-SAMs versus ODS-SAMs at different molecular areas. The dotted lines are the experimental surface-potential values measured by KPFM. Reprinted from [73].

ture. The HBCs were found to arrange in the film in two different phases: one characterized by a low-pressure packing in which the aromatic cores of the HBCs were stacked in order to maximize the overlap of the π -orbitals and a second, more dense phase where the alkyl chains were organized in a crystalline fashion and the aromatic cores separated by a larger distance, i.e., characterized by a lower overlap of the π -orbitals.^[74] The authors proposed that the electrons can be considered delocalized along the π -stack of the former phase, while in the second phase the electrons should be regarded as highly localized on the molecules since the coherence in the π -stack is lost. When the two phases are brought into contact, the more loosely bound electrons lying high in the “conduction” band of the low-pressure phase will be attracted by the more

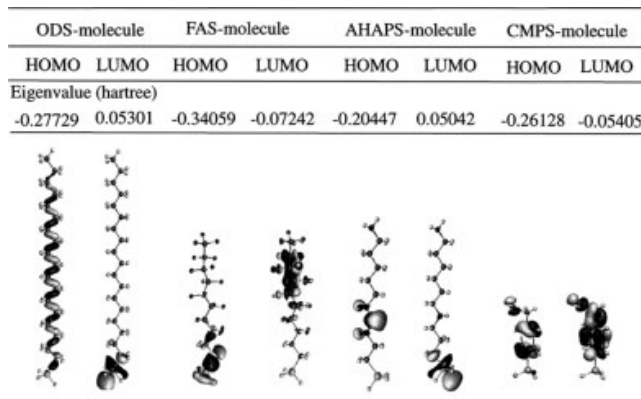


Figure 12. Schematic drawings of the HOMO and LUMO for the ODS, FAS, AHAPS, and CMPS molecules, along with their eigenvalues. Reprinted from [73].

tightly bound molecular orbitals in the high-pressure phase. As a result, a small amount of electrons will be funneled from the low- to the high-pressure domains. This will lead to slightly more positive low-pressure areas and slightly more negative high-pressure domains, compatible with the representation of a p–n junction (Fig. 13). The measured potential difference of 20 mV between the high- and low-pressure phases is in good agreement with typical bandwidth values of π -stacks.^[74]

Similar results were obtained by investigating the structural and electronic properties of different submicrometer-scale self-assembled architectures of a larger alkylated synthetic nanographene consisting of 96 carbons in the aromatic core (C₉₆-C₁₂).^[75] Extended layers, percolated networks, and broken patterns were grown from solutions at surfaces and successfully visualized by KPFM (Fig. 14).^[76] This study made it possible to determine the local ϕ of the different π -conjugated nanostructures adsorbed on mica with a resolution below 10 nm and 0.05 eV. It revealed that the ϕ strongly depends on the local molecular order at the surface, and in particular on the delocalization of electrons in the π -states, on the molecular orientation at surfaces, on the molecular packing density, on the presence of defects in the film, and on the different conformations of the aliphatic peripheral chains that might cover the conjugated core. These results were confirmed by comparing the KPFM estimated local ϕ of layers supported on mica, where the molecules are preferentially packed “edge-on” on the substrate, with the UPS microscopically measured ϕ of layers adsorbed on graphite, where the molecules should tend to assemble “face-on” on the surface. It appears that local ϕ studies are of paramount importance to understand the electronic properties of active organic nanostructures.^[76]

KPFM has also been exploited to study complex biological architectures such as DNA. Contact-potential difference images revealed DNA strands oriented on Si and glass substrates, recorded using a hexadecanethiol-modified gold tip, although without achieving a particularly high resolution.^[77]

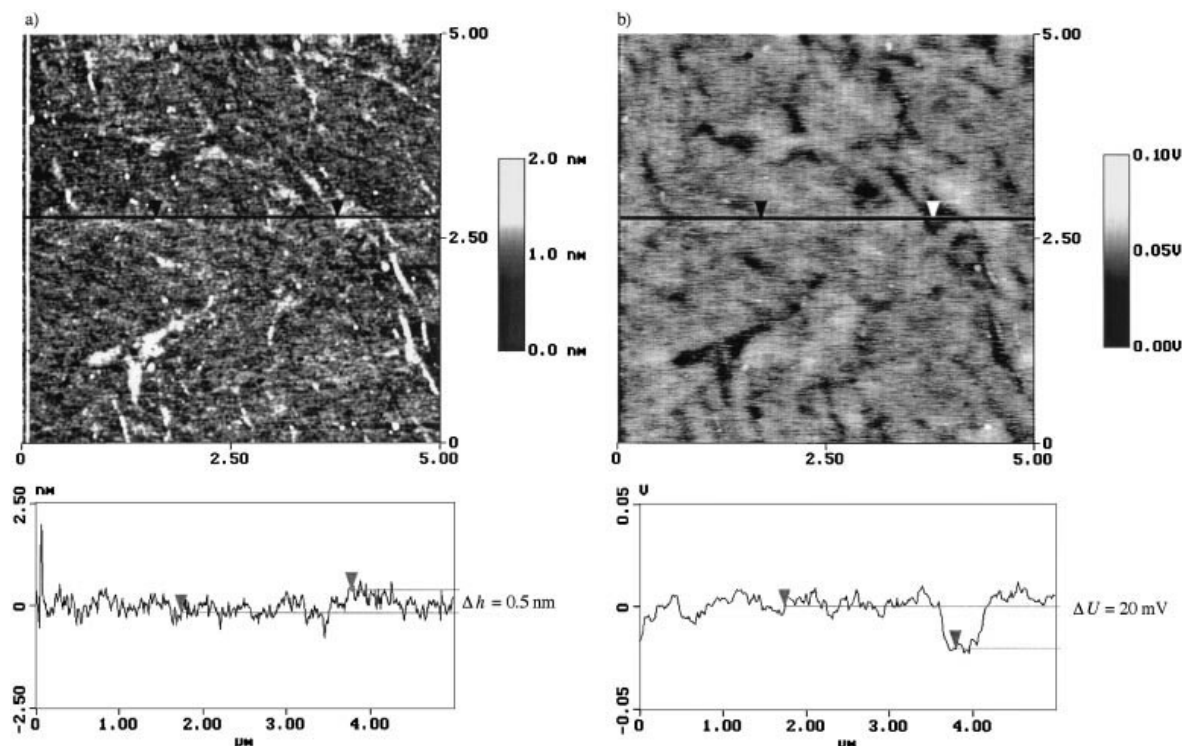


Figure 13. a) SFM tapping-mode topography image of a LB monolayer of HBC transferred to a SiO_x at a mean area per molecule $A = 1 \text{ nm}^2$. A cross-section profile from the middle of the scan is also displayed, showing the height difference between the high-pressure and the low-pressure phases. The height difference is ca. 0.5 nm. b) KPFM image showing the potential landscape of the same area shown in (a). The potential of the low-pressure phase is ca. 20 mV higher than the potential of the high-pressure phase, as can be also seen from the cross-section profile. Reprinted from [74].

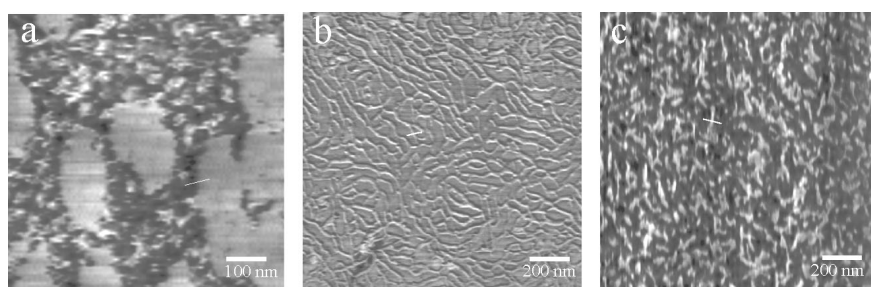


Figure 14. KPFM image of C96- C_{12} architectures on mica: a) layers, b) network of fibers, and c) elongated agglomerates. Different profiles have been traced on the KPFM images in order to estimate the local work functions (not shown). The white line in each image shows an example of a location where the profiles were traced. Reprinted from [76].

KPFM also permits the exploration of dynamic properties of single molecules. As an example, the changes of potential in photosynthetic structural proteins during light harvesting were monitored with a minimal interference in the protein activity. This study addressed a biological nanometer-sized supramolecular structure called photosystem I (PS I), which can be isolated and purified from green plants. By means of KPFM, measurement of exogenous photovoltages generated from single PS I reaction centers in a heterostructure composed of PS I, organosulfur molecules, and atomically flat gold were carried out.^[78]

PS I adsorbs with a preferential orientation, keeping its electron-acceptor center on the side away from the substrate. KPFM measurements performed in a helium atmosphere with the lift-off technique allowed, with a remarkably high resolution, quantification of the potential of this acceptor center. By irradiating the sample with visible light, the photosynthetic process triggers a photon-induced charge separation, negatively biasing the acceptor center. The bias shift, being ca. 1 V, can be easily measured in real time with KPFM. Furthermore, a 2D map of the protein surface potential was achieved with KPFM, providing information on the position

of the acceptor center inside the protein. The obtained results are in good agreement with the known structural and energetic features of protein PS I measured using other techniques (Fig. 15).^[78]

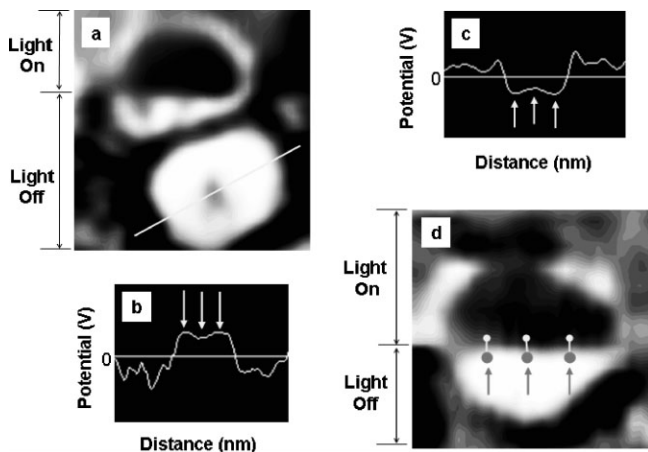


Figure 15. KPFM images of individual PS I reaction centers and corresponding cross-sectional voltage–distance profiles. a) View of two PS I reaction centers: the lower PS I was imaged entirely in darkness, whereas the upper PS I was imaged mostly in light. Note the abrupt change in electric potential for the upper PS I as the diode laser was switched off in mid-scan at the indicated location. b) Light-off voltage–distance profile along the indicated cross-sectional axis. c) Light-on voltage–distance profile. d) A single PS I was “bisected” in mid-scan by switching the diode laser off. Voltage-difference measurements in light and darkness, indicated by the proximal dots, were taken at the peripheries and the center. Reprinted with permission from [78]. Copyright 2000 American Chemical Society.

KPFM also granted insight into the photochemical behavior of chemisorbed organic layers at surfaces. Organosilane layers ($\text{R-Si}(\text{OCH}_3)_3$), where R can be either an aliphatic or an aromatic group, have been patterned on SiO_x wafers and then decomposed using UV radiation. The surface-potential difference between the nanopatterned irradiated and non-irradiated areas has been measured by KPFM.^[79] The occurrence of a photo-oxidation of the methyl end groups transformed them in CHO and COOH, and the subsequent complete molecular decomposition of the organic monolayer led to changes in the surface potential which were highlighted by KPFM, XPS, and lateral-force microscopy. The change in surface potential in these systems is due to the variation of the molecular dipole moment, as confirmed by ab-initio calculations.^[80]

In a similar set of experiments, KPFM was able to monitor macroscopically the light-induced dipole-moment changes due to cis–trans molecular rearrangement in SAMs of thiol-azobenzenes on Au (111).^[81]

A well-known class of molecules with a great potential for organic-electronics applications are poly(thiophenes). KPFM studies provided unambiguous evidence for the dependence of the measured work function of the molecular material on the substrate type. Monolayers and bilayers of dimethylquinquethiophene supported on Pt and Ta substrates displayed

surface-potential differences of 5.36 V and 3.92 V, respectively. These values are similar to those of the underlying metals.^[82] The difference in surface potential has been interpreted assuming a charge transfer from the metal to the thiophene, and a reduction of quinquethiophene LUMO due to image force interactions. The deposition on Pt of a second quinquethiophene layer led to an increase of 0.1 V in the measured potential. This was explained by an induced polarization due to the local electric field originating from the charges exchanged between the first layer and the metal. A decrease of the measured potential down to only 20 mV above the potential of the Pt background was observed upon irradiating the quinquethiophene with visible light. This behavior is due to transfer of photogenerated holes from the molecule to the substrate because of the local electric field.^[83]

7. KPFM on Organic-Electronics Devices

KPFM, being a non-contact technique, can be employed to explore in a non-invasive way the electronic and morphological behavior of working devices based on molecular organic materials or polymers. Understanding and controlling the relation between the electronic-transport properties and the morphology of conducting organic layers is crucial for further development and exploitation of these materials as many aspects, including their poor electronic properties due to the polycrystalline character of the organic thin films, often limit the overall performance of the devices.

The tailoring of a metal/organic interface represents a fundamental issue in the study and optimization of working devices, such as light-emitting diodes (LEDs), field-effect transistors (FETs), and solar cells. Extensive investigation revealed that the contact resistance at the metal/organic interface depends on many factors, including the work function of the metal, the ionization potential of the organic architecture, the effect of the diffusion layer, and the built-in potential at the interface.^[84] Moreover, as pointed out in Section 4, the metal/organic interface is a quite complex system as it involves controversial issues such as vacuum-level shift, band bending, and interface-dipole formation. KPFM allows potential differences at the interface between different components to be followed, providing 2D maps of potential drops due to low-conductivity areas, short circuits, electrical defects, and phase separations.

Notably, Sirringhaus, Friend, and co-workers performed quantitative investigations with KPFM measuring the potential drop along source/channel/drain interfaces in different organic-based transistors while current was flowing through the device.^[47,84–86]

The obtained potential decay in a 5.2 μm wide poly(hexylthiophene) (P3HT) transistor allowed the estimation of the resistances of the source and drain contacts, the charge mobility, and the resistance of the polymer architecture, as well as the linear and non-linear transistor operating ranges (Figs. 16,17).^[47,86]

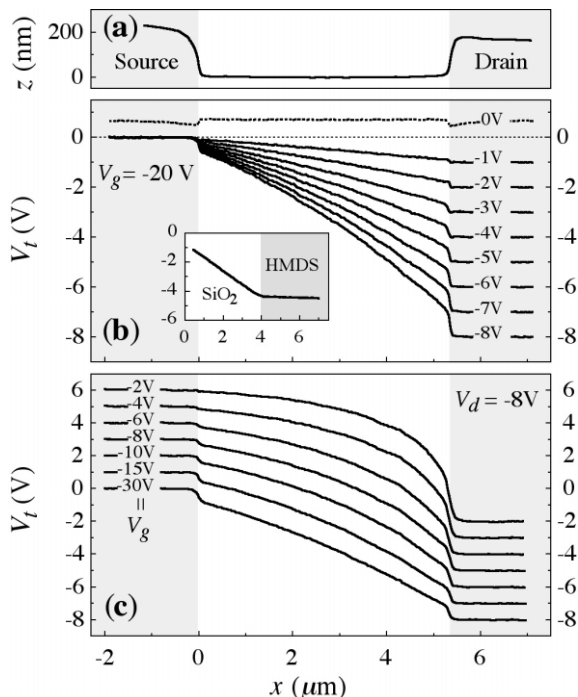


Figure 16. KPFM of a P3HT thin-film field-effect transistor (channel length $L=5.2 \mu\text{m}$). 2D maps were recorded, but only profiles perpendicular to the channel are shown since the conductivity of P3HT proved to be homogeneous. It is worth noting that interchanging source and drain did not change the results. a) The channel between source and drain electrodes is clearly seen in the topographic profile (x denotes the distance from the source). b) Potential profiles acquired simultaneously with the topography at $T=300 \text{ K}$. The gate voltage was kept constant at $V_g=-20 \text{ V}$ while the drain voltage V_d was decreased from -1 to -8 V in -1 V steps ($I_d=3.9, 7.6, 11.0, 14.2, 17.2, 20.1, 22.8$, and $25.4 \mu\text{A}$). $\Delta\Phi(x)$, i.e., the profile for $V_d=0 \text{ V}$ (dotted line, offset by 0.5 V for clarity), was subtracted from all profiles with $V_d \neq 0$. c) Potential profiles as a function of gate voltage, where $V_d=-8 \text{ V}$ and $T=165 \text{ K}$. (Profiles are offset by increasing 1 V steps: $I_d=4010, 850, 334, 195, 97, 37$, and 9 nA). Inset of (b): Potential profile of an $L=20 \mu\text{m}$ P3HT transistor with partially hexamethyldisilazane (HMDS) covered SiO_2 interface ($V_g=-40 \text{ V}$, $V_d=-5 \text{ V}$, and $T=300 \text{ K}$). The lateral electric field (i.e., $-\partial V_t/\partial x$) in the bare- SiO_x region is 26 times larger than the value found in the HMDS region, indicating that the field-effect mobility of a HMDS-treated interface is ~ 20 times the one of bare SiO_x , in excellent agreement with field-effect mobilities deduced from devices made of either bare or completely HMDS-treated SiO_x surfaces. Reprinted with permission from [47]. Copyright 2002 American Institute of Physics.

The contact resistance at the P3HT/Au electrode interface is

$$R_C = W(\Delta V_s + \Delta V_d)/I_d \quad (20)$$

where W is the channel width and I_D is the current passing through the device. Potential drops ΔV_s and ΔV_d at source and drain interfaces, respectively, were measured with KPFM.

From the potential's profile across the active layer, the field-effect mobility μ of the organic material was obtained using

$$I_D = e W n(x) \mu(V_g', E) E(x) \quad (21)$$

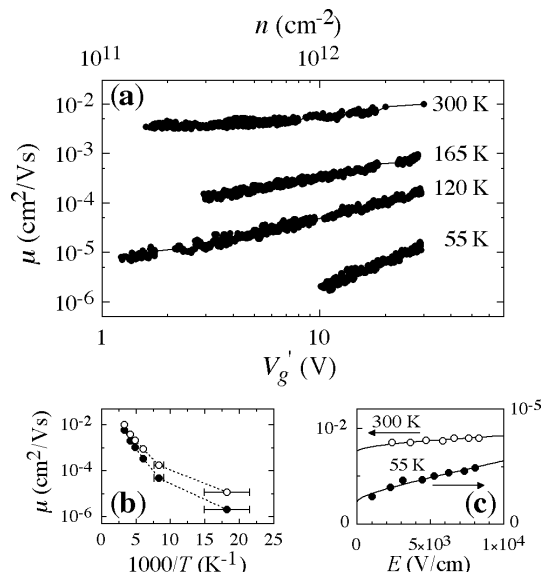


Figure 17. Field-effect hole mobility of regioregular head-to-tail P3HT. a) Dependence on effective gate voltage, i.e., carrier concentration. b) Temperature dependence. Open and filled symbols represent data for gate potentials $V_g'=30 \text{ V}$ and 10 V , respectively. c) Dependence on lateral electric field ($V_g'=20 \text{ V}$). The continuous lines depict a fit with a Poole-Frenkel law: $\mu \propto \exp(B\sqrt{E}/kT)$ with $B=5 \times 10^{-5} \text{ eV (V cm}^{-1})^{-1/2}$. Reprinted with permission from [47]. Copyright 2002 American Institute of Physics.

$$E(x) = -\partial V(x)/\partial x \quad (22)$$

where V_g is the gate voltage.

The density n of field-induced carriers is given by $en(x) = C_i V_g'$, while $V_g' = V(x) - V_g$ is the effective potential drop over the insulator and C_i is the insulator capacitance. In the non-linear mode ($V_d > V_g$), the density of accumulated charges decreases when going from source to drain, and the mobility decreases as well. This is a nice example of how the analysis of KPFM measurements allows complete characterization of the electrical properties of an operating electronic device.

In a different set of experiments, the absolute work function value of the aforementioned P3HT was estimated by KPFM, UPS, and photoemission electron spectroscopy, and compared to the work functions of the electrodes wiring the P3HT. In this case, the organic material was deposited on a flexible substrate (i.e., paper) and wired using unconventional electrodes made of colloidal graphite and carbon black, patterned on the paper using a commercial plotter. The work functions measured in vacuum amounted to 3.8 eV , 4.1 eV , and 3.8 eV , for P3HT, graphite, and carbon black, respectively. This shows how the versatility and applicability of KPFM allows the study of unconventional working devices, in this case fabricated on an unusual substrate.^[87] KPFM can be used as well to explore charge transport through domain boundaries in polycrystalline organic layers. Channel-potential drops in transistors based on a nematic glassy-state poly-

mer revealed that domain boundaries do not limit the charge transport.^[86] It is, rather, the transport through the domains themselves that is the main obstacle for the current flow.^[86] Qualitative KPFM measurements of potential drops at domain boundaries due to different molecular orientation have also been performed on very thin Langmuir–Blodgett polymer layers (Fig. 18).^[88]

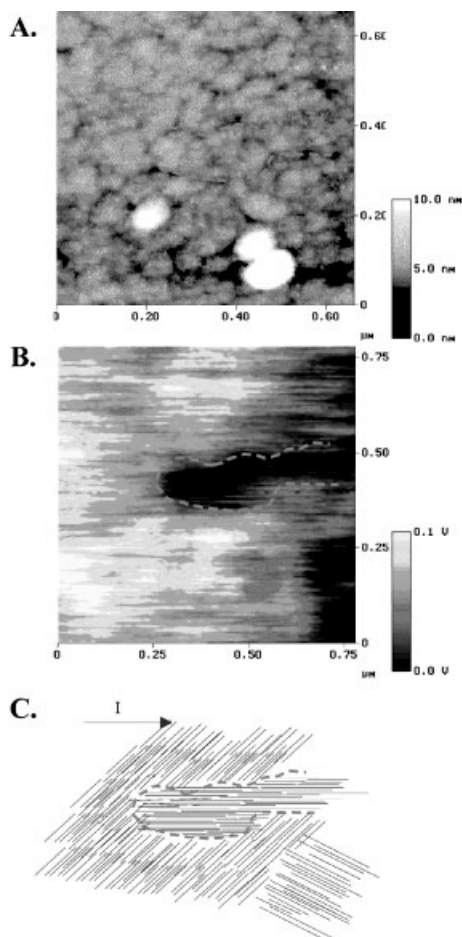


Figure 18. A) Tapping-mode SFM topographical map of a Langmuir–Blodgett polymer monolayer. B) EFM measured potential map of the same sample area visualized in (A). The structure (marked by a dashed line) that correlates to the domain seen in the EFM picture is clearly visible in the height profile. Other features, such as the two dust particles (white area in the height picture), can also be seen in the EFM picture. C) A model of how the polymer crystallites could be oriented in order to give rise to the potential map observed. Please note that the lines do not represent individual polymers, but are drawn to indicate the possible direction of the highly oriented polycrystallites, which form the “electronic” domains. Reprinted from [88].

A detailed study on the importance of source–drain contacts in organic devices was recently reported by Frisbie and co-workers.^[89] Surface potentials of operating pentacene thin-film FETs with two different contact geometries (deposited above or beneath the active organic layer) were mapped by KPFM. The surface-potential distribution was used to quanti-

fy the potential drops at the source and drain contacts. The bottom-contact FETs were contact limited at large gate voltages, while the top-contact FETs were not contact limited. In both geometries, the contact and the channel resistances decreased notably with the increasing (negative) gate bias but did not depend strongly on the drain bias. This study highlighted the potential of KPFM to monitor the charge-transport bottlenecks in operating pentacene devices, and more generally to correlate the electrical behavior with the structure of the devices by comparing the surface potential to the topographic maps (Figs. 19,20).

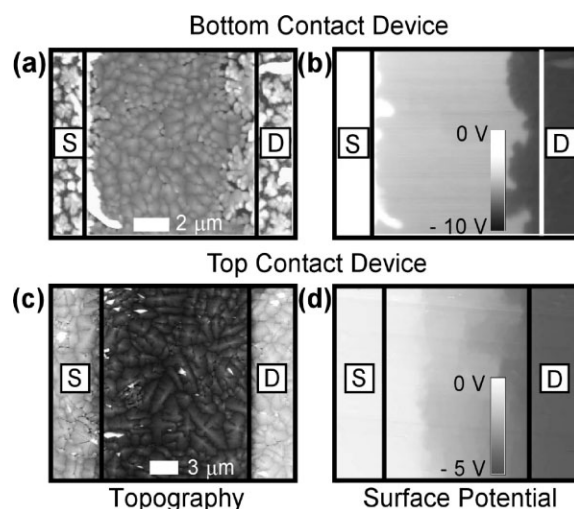


Figure 19. a,c) Topographic and b,d) corresponding surface-potential images for bottom-contact and top-contact thin-film FETs. Drain biases were $V_D = -10$ V for (b) and $V_D = -5$ V for (d), and gate biases were $V_G = 0$ V for both cases. Labels S and D indicate the source and drain electrodes, respectively. The solid vertical lines indicate the edge between the contacts and the conducting channel. Reprinted with permission from [89]. Copyright 2003 American Institute of Physics.

A proper choice of the metallic electrode is needed, since the resistance at the metal/organic interface is dependent on the metal type. For pentacene-based junctions, contacts with platinum showed a very small resistance compared with palladium and nickel.^[90]

The better efficiency of Pt was also observed for a FET fabricated using a monolayer of methylquinqueithiophene.^[91] In this work, the resistance in the channel and at the source/drain interface was measured. Despite the nominal thickness of a single layer of the active film, a uniform potential drop and high-resistivity sites corresponding to interfaces and defects, respectively, were clearly observed and discussed (Fig. 21).^[91]

Nanotube-based transistors have recently gathered much interest. The electrical characterization of these devices has been quite complex, as the semiconducting nanotubes behave as p-type or n-type if they are measured in air or vacuum, respectively. KPFM measurements on Au-nanotube-Au systems, using only semiconducting single-wall nanotubes, demonstrated that the p-type behavior in air is due to oxygen ad-

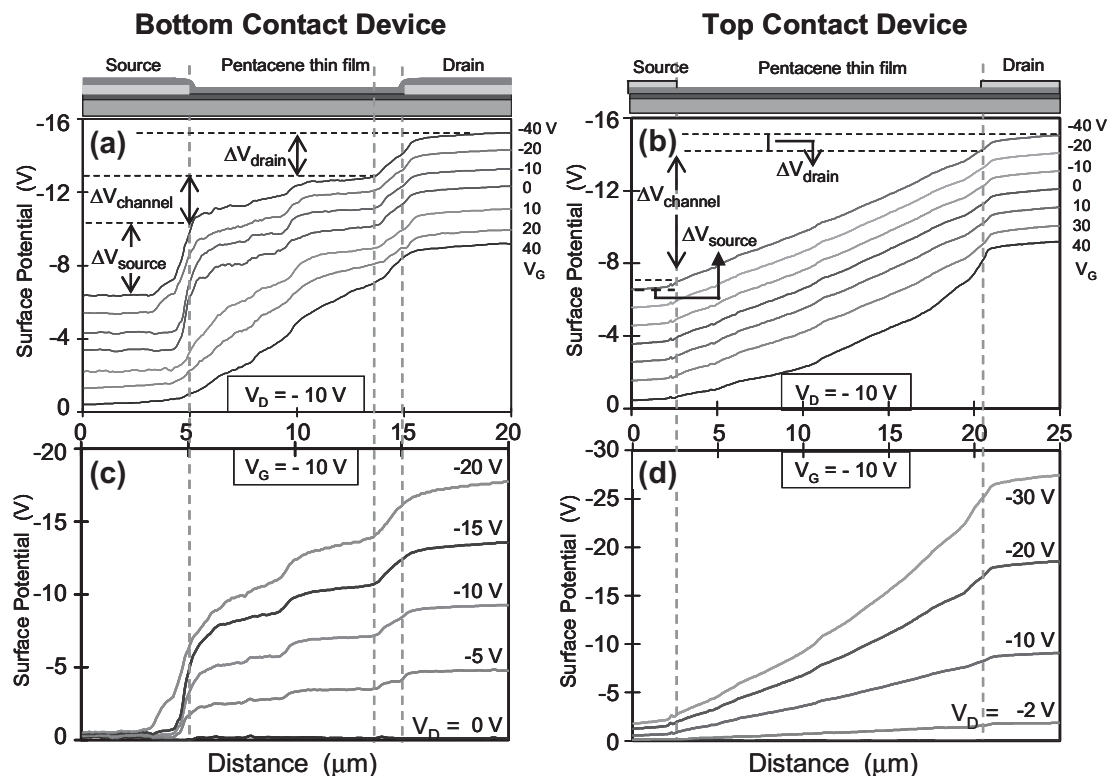


Figure 20. a,c) A set of surface potential profiles for a bottom-contact thin-film FET with a schematic of the device shown at the top for reference. For (a), $V_D = -10\text{ V}$ and $V_G = 40$ to -40 V . The profiles are artificially offset for clarity of viewing. For (c), $V_G = -10\text{ V}$ and $V_D = 0$ to -20 V . The channel length, as defined by the lithography, is $10\text{ }\mu\text{m}$. The outer dashed lines indicate the edge between the contacts and the channel. b,d) A similar set of profiles for a top-contact FET. In this case, the channel length was $\sim 18\text{ }\mu\text{m}$. The profiles in each device were taken at the same spot in the channel. Zero-bias profiles were not subtracted from any of the data shown here. Reprinted with permission from [89]. Copyright 2003 American Institute of Physics.

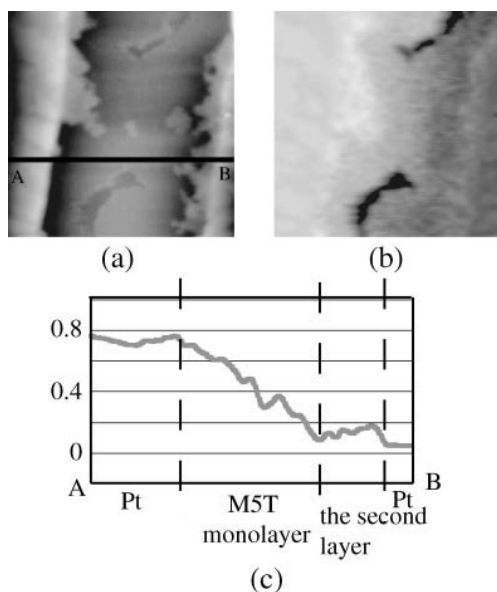


Figure 21. Methylquinethiophene monolayer partially covering the gap. a) Topographic image and b) surface-potential image with 0.7 V DC voltage applied. c) Surface-potential line profile along A–B in (a). Reprinted with permission from [91]. Copyright 2003 Institute of Pure and Applied Physics.

sorbing on the Au surface, creating a dipole layer and thus changing the Au work function. The dipole formation can be hindered by simple “passivation” of the Au surface using H_2S or alkanethiols.^[59]

As in the case of inorganic solar cells, organic photovoltaic devices can also be studied with KPFM under illumination. Very recently, the surface potential of polymer heterojunction solar cells based on a blend of a poly(*p*-phenylene-vinylene) (PPV) and fullerene has been measured. Under proper conditions, the fullerenes segregate into a PPV matrix, forming spherical clusters which can be visualized by SFM. KPFM images of the blend showed that some clusters possess a work function higher than the surrounding polymer, while other clusters have a lower work function. SEM measurements revealed that the clusters with the lower work function are electron-rich fullerene aggregates directly exposed to the atmosphere, while those with the lower work function are covered by a thin layer of polymer. This thin layer limits photocurrent collection, and thus device efficiency.^[92]

Photoinduced charge generation in polyfluorene-based photovoltaic structures has also been studied by KPFM. The high lateral resolution of the technique recently allowed the characterization of the three-dimensional structure of thin films of blends of poly(9,9'-dioctylfluorene-*co*-benzothiadiaz-

zole) (F8BT) and poly (9,9'-dioctylfluorene-*co*-bis-*N,N'*-(4-butylphenyl)-bis-*N,N'*-phenyl-1,4-phenylenediamine) (PFB). Very interestingly, from the strong correlation between surface photovoltage and blend morphology, a simple model for the lateral and vertical film structure has been proposed, identifying in particular those regions with the most efficient conduction pathway for the photocurrent.^[93]

KPFM measurements under dark and illumination conditions have been also used to study qualitatively the charge-trap release in poly[(9,9'-dioctylfluorene-2,7-diyl)-*alt*-phenylene-(*N*-(*p*-2-butylphenyl)imino-phenylene)] (TFB). The surface density of charges is shown to decay slowly in the dark, due to the discharging of shallow traps, and to reach a steady value, stable over time, due to deep-level traps which remain charged in the dark. Upon illumination, the charge density, and thus the measured potential, quickly drops to zero. The trap discharging only takes place with light of $\lambda < 450$ nm, and it is faster if shorter wavelengths are used (Fig. 22).^[86]

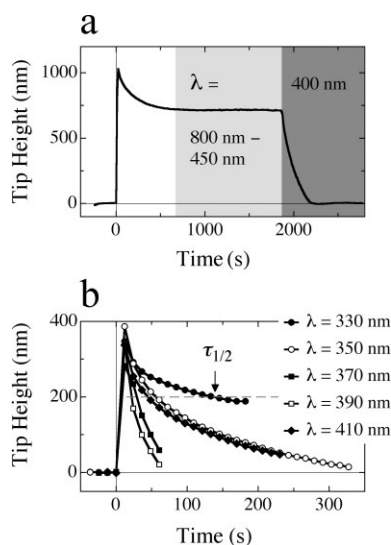


Figure 22. Photon-assisted release of trapped charges in a TFB transistor. The measurements were recorded in the center of the transistor channel. a) Only illumination with light of $\lambda < 450$ nm results in trap release. b) The process of trap release depends critically on the wavelength of the incident light. Reprinted with permission from [86]. Copyright 2004 Elsevier.

The use of KPFM to study working devices is not limited to steady-state conditions; transient potentials can be measured as well, with a time resolution ~ 5 ms. The charging and discharging of the active organic layer of a transistor can be followed with KPFM while the applied gate voltage is varied. Changes in potential at each point of the active layer reveal an exponential decay which depends on the dimension of the device, the final gate voltage, and the field-effect mobility. Therefore, KPFM also provides tools to measure field mobility in organic materials.^[85,86]

The density of trapped charges in defects of organic layers can be also estimated by a KPFM-based approach.^[86] The

traps are first accumulated in the layer by applying a gate voltage larger than the turn-on voltage. Then, the gate is brought below the turn-on voltage. This drives all the mobile charges out of the layer, and leaves only trapped, immobile charges inside the organic architecture. The interaction of the tip with the charged defects can be used to measure charge density.^[86]

Unfortunately, it should be pointed out that the KPFM technique is not fast enough to detect shallow traps, which discharge too fast for KPFM detection. Trap densities down to 10^9 cm⁻², corresponding to a change in tip potential of about 10 mV, can be resolved in principle.^[86]

8. Conclusions and Future Challenges

This review highlighted the potential of Kelvin probe force microscopy to gain insight into the structural and electronic properties simultaneously of functional surfaces and interfaces. The versatility of the technique makes it possible to perform measurements under different environmental conditions on different sample types, including metals and inorganic and organic materials. Such explorations can be accomplished with resolutions of a few nanometers and some millivolts. This is of great importance, since it is well established that a solid surface possesses different properties from the bulk material. Of equal importance, there are many processes of technological significance which depend upon the use of solid surfaces and which may be improved in some way if the role of the surface and the interface could be fully understood. Beyond imaging, KPFM is a viable approach to get new information concerning electrical and electronic properties of sample surfaces.

KPFM is a powerful technique to study, in a non-invasive way, complex electronic phenomena in supramolecular engineered systems and devices. The combination of such a methodology with external stimuli, such as light irradiation, opens new doors to the exploration of processes occurring in nature or in artificial complex architectures.

Unfortunately, surface effects (e.g., dipole formation), as well as systematic errors due to the simple geometrical models often assumed to interpret tip-sample interactions, still affect KPFM measurements and data interpretation. Indeed, various approximations are sought whose complexity depends on the variables taken into account. Moreover, the different information that can be attained from the distinct KPFM signals still needs to be fully unraveled. By combining this information, KPFM can acquire a wide knowledge of the overall electronic and electrical behavior of a sample surface: work function, capacitance, interface electronic behavior, and mobile charge-carrier concentration can be determined in this way. Therefore, KPFM is a powerful technique, not only for exploring electronic (dynamic) properties of materials, but also for optimizing the design and performance of new devices based on organic-semiconductor nanostructures.

Received: July 8, 2005

Final version: August 10, 2005

Published online: December 8, 2005

- [1] S. R. Forrest, *Nature* **2004**, 428, 911.
- [2] G. Binnig, C. F. Quate, C. Gerber, *Phys. Rev. Lett.* **1986**, 56, 930.
- [3] C. Bustamante, D. Keller, *Phys. Today* **1995**, 48, 32.
- [4] H. Takano, J. R. Kenseth, S.-S. Wong, J. C. O'Brien, M. D. Porter, *Chem. Rev.* **1999**, 99, 2845.
- [5] P. Samorì, *J. Mater. Chem.* **2004**, 14, 1353.
- [6] G. Binnig, H. Rohrer, C. Gerber, E. Weibel, *Appl. Phys. Lett.* **1982**, 40, 178.
- [7] J. K. Gimzewski, C. Joachim, *Science* **1999**, 283, 1683.
- [8] D. A. Bonnell, R. Shao, *Curr. Opin. Solid State Mater. Sci.* **2003**, 7, 161.
- [9] T. W. Kelley, E. L. Granström, C. D. Frisbie, *Adv. Mater.* **1999**, 11, 261.
- [10] J. R. Matey, J. Blanc, *J. Appl. Phys.* **1985**, 57, 1437.
- [11] B. D. Terris, J. E. Stern, D. Rugar, H. J. Mamin, *Phys. Rev. Lett.* **1989**, 63, 2669.
- [12] M. Nonnenmacher, M. P. O'Boyle, H. K. Wickramasinghe, *Appl. Phys. Lett.* **1991**, 58, 2921.
- [13] C. Gomez-Navarro, F. Moreno-Herrero, P. J. de Pablo, J. Colchero, J. Gomez-Herrero, A. M. Baro, *Proc. Natl. Acad. Sci. USA* **2002**, 99, 8484.
- [14] L. E. Cheran, M. E. McGovern, M. Thompson, *Faraday Discuss.* **2000**, 116, 23.
- [15] A. Kikukawa, S. Hosaka, R. Imura, *Rev. Sci. Instrum.* **1996**, 67, 1463.
- [16] L. Kelvin, *Philos. Mag.* **1898**, 46, 82.
- [17] H. M. Rosenberg, *The Solid State*, Clarendon, Oxford, UK **1975**.
- [18] M. Prutton, *Introduction to Surface Physics*, Oxford University Press, New York **1994**.
- [19] W. A. Zisman, *Rev. Sci. Instrum.* **1932**, 3, 367.
- [20] L. Kronik, Y. Shapira, *Surf. Sci. Rep.* **1999**, 37, 1.
- [21] D. K. Schroder, *Meas. Sci. Technol.* **2001**, 12, R16.
- [22] *Nanoscope IV Controller Manual*, Veeco, Woodbury, NY **2002**.
- [23] H. O. Jacobs, P. Leuchtmann, O. J. Homan, A. Stemmer, *J. Appl. Phys.* **1998**, 84, 1168.
- [24] G. Koley, M. G. Spencer, H. R. Bhangale, *Appl. Phys. Lett.* **2001**, 79, 545.
- [25] O. Cherniavskaya, L. Chen, V. Weng, L. Yuditsky, L. E. Brus, *J. Phys. Chem. B* **2003**, 107, 1525.
- [26] J. Colchero, A. Gil, A. M. Baró, *Phys. Rev. B: Condens. Matter Mater. Phys.* **2001**, 64, 245403.
- [27] T. Takahashi, S. Ono, *Ultramicroscopy* **2004**, 100, 287.
- [28] A. Gil, J. Colchero, J. Gomez-Herrero, A. M. Baró, *Nanotechnology* **2003**, 14, 332.
- [29] C. H. Lei, A. Das, M. Elliott, J. E. Macdonald, *Nanotechnology* **2004**, 15, 627.
- [30] T. Takahashi, T. Kawamukai, *Ultramicroscopy* **2000**, 82, 63.
- [31] O. Cherniavskaya, L. Chen, M. A. Islam, L. Brus, *Nano Lett.* **2003**, 3, 497.
- [32] U. Zerweck, C. Loppacher, T. Otto, S. Grafström, L. M. Eng, *Phys. Rev. B: Condens. Matter Mater. Phys.* **2005**, 71, 125424.
- [33] K. Okamoto, Y. Sugawara, S. Morita, *Jpn. J. Appl. Phys., Part 1* **2003**, 42, 7163.
- [34] C. Sommerhalter, T. Glatzel, T. W. Matthes, A. Jäger-Waldau, M. C. Lux-Steiner, *Appl. Surf. Sci.* **2000**, 157, 263.
- [35] S. M. Sze, *Physics of Semiconductor Devices*, 2nd ed., Wiley, New York **1981**.
- [36] H. Ishii, H. Oji, E. Ito, N. Hayashi, D. Yoshimura, K. Seki, *J. Lumin.* **2000**, 87–89, 61.
- [37] H. Ishii, N. Hayashi, E. Ito, Y. Washizu, K. Sugi, Y. Kimura, M. Niwano, Y. Ouchi, K. Seki, *Phys. Status Solidi A* **2004**, 201, 1075.
- [38] M. Pfeiffer, K. Leo, N. Karl, *J. Appl. Phys.* **1996**, 80, 6880.
- [39] H. Ishii, K. Sugiyama, E. Ito, K. Seki, *Adv. Mater.* **1999**, 11, 605.
- [40] K. C. Kao, *Electrical Transport in Solids*, Pergamon, Oxford, UK **1981**.
- [41] M. Schott, in *Organic Conductors: Fundamentals and Applications* (Ed: J. P. Farges) Marcel Dekker, New York **1994**, p. 539.
- [42] D. P. Woodruff, T. A. Delchar, *Modern Techniques of Surface Science*, Cambridge University Press, Cambridge, UK **1986**.
- [43] J. Hölzel, F. K. Schulte, H. Wagner, *Solid Surface Physics*, Springer, Berlin **1979**.
- [44] P. Nielsen, *Photogr. Sci. Eng.* **1974**, 18, 186.
- [45] K. Wandelt, *Thin Metal Films and Gas Chemisorption* (Ed: P. Wissman), Elsevier, Amsterdam, The Netherlands **1987**.
- [46] K. Seki, N. Hayashi, H. Oji, E. Ito, Y. Ouchi, H. Ishii, *Thin Solid Films* **2001**, 393, 298.
- [47] L. Bürgi, H. Sirringhaus, R. H. Friend, *Appl. Phys. Lett.* **2002**, 80, 2913.
- [48] A. Alessandrini, U. Valdrè, *Philos. Mag. Lett.* **2003**, 83, 441.
- [49] A. K. Henning, T. Hochwitz, J. Slinkman, J. Never, S. Hoffmann, P. Kaszuba, C. Daghlán, *J. Appl. Phys.* **1995**, 77, 1888.
- [50] G. H. Buh, H. J. Chung, C. K. Kim, J. H. Yi, I. T. Yoon, Y. Kuk, *Appl. Phys. Lett.* **2000**, 77, 106.
- [51] A. Doukali, S. Ledain, C. Guasch, J. Bonnet, *Appl. Surf. Sci.* **2004**, 235, 507.
- [52] T. Meoded, R. Shikler, N. Fried, Y. Rosenwaks, *Appl. Phys. Lett.* **1999**, 75, 2435.
- [53] R. Shikler, N. Fried, T. Meoded, Y. Rosenwaks, *Phys. Rev. B: Condens. Matter Mater. Phys.* **2000**, 61, 11041.
- [54] T. Yamauchi, M. Tabuchi, A. Nakamura, *Appl. Phys. Lett.* **2004**, 84, 3834.
- [55] M. A. Salem, H. Mizuta, S. Oda, *Appl. Phys. Lett.* **2004**, 85, 3262.
- [56] A. Chavezpíerson, O. Vatel, M. Tanimoto, H. Ando, H. Iwamura, H. Kanbe, *Appl. Phys. Lett.* **1995**, 67, 3069.
- [57] G. Lèveque, P. Girard, E. Skouri, D. Yarekha, *Appl. Surf. Sci.* **2000**, 157, 251.
- [58] C. Maeda, S. Kishimoto, T. Mizutani, T. Sugai, H. Shinohara, *Jpn. J. Appl. Phys., Part 1* **2003**, 42, 2449.
- [59] X. D. Cui, M. Freitag, R. Martel, L. Brus, P. Avouris, *Nano Lett.* **2003**, 3, 783.
- [60] R. Grover, B. McCarthy, Y. Zhao, G. E. Jabbour, D. Sarid, G. M. Laws, B. R. Takulapalli, T. J. Thornton, D. Gust, *Appl. Phys. Lett.* **2004**, 85, 3926.
- [61] S. Takahashi, T. Kishida, S. Akita, Y. Nakayama, *Jpn. J. Appl. Phys., Part 1* **2001**, 40, 4314.
- [62] C.-S. Jiang, H. R. Moutinho, F. S. Hasoon, H. A. Al-Thani, D. J. Friedman, J. F. Geisz, Q. Wang, M. J. Romero, M. M. Al-Jassim, in *Proc. NCPV and Solar Program Review Meeting*, National Renewable Energy Laboratory, Golden, CO **2003**, p. 870.
- [63] C.-S. Jiang, D. J. Friedman, J. F. Geisz, H. R. Moutinho, M. J. Romero, M. M. Al-Jassim, *Appl. Phys. Lett.* **2003**, 83, 1572.
- [64] C.-S. Jiang, R. Noufi, K. Ramanathan, J. A. AbuShama, H. R. Moutinho, M. M. Al-Jassim, *Appl. Phys. Lett.* **2004**, 85, 2625.
- [65] C.-S. Jiang, R. Noufi, J. A. AbuShama, K. Ramanathan, H. R. Moutinho, J. Pankow, M. M. Al-Jassim, *Appl. Phys. Lett.* **2004**, 84, 3477.
- [66] S. Sadewasser, T. Glatzel, S. Schuler, S. Nishiwaki, R. Kaigawa, M. C. Lux-Steiner, *Thin Solid Films* **2003**, 431, 257.
- [67] A. Ulman, *Introduction to Ultrathin Organic Films*, Academic, San Diego, CA **1991**.
- [68] G. E. Poirier, *Chem. Rev.* **1997**, 97, 1117.
- [69] E. Delamarche, B. Michel, H. A. Biebuyck, C. Gerber, *Adv. Mater.* **1996**, 8, 719.
- [70] T. Ichii, T. Fukuma, K. Kobayashi, H. Yamada, K. Matsushige, *Nanotechnology* **2004**, 15, S30.
- [71] J. Lü, E. Delamarche, L. Eng, R. Bennewitz, E. Meyer, H. J. Güntherodt, *Langmuir* **1999**, 15, 8184.
- [72] H. McNally, D. B. Janes, B. Kasibhatla, C. P. Kubiak, *Superlattices Microstruct.* **2002**, 31, 239.
- [73] N. Saito, K. Hayashi, H. Sugimura, O. Takai, N. Nakagiri, *Surf. Interface Anal.* **2002**, 34, 601.
- [74] N. Reitzel, T. Hassenkam, K. Balashev, T. R. Jensen, P. B. Howes, K. Kjaer, A. Fechtenkötter, N. Tchebotareva, S. Ito, K. Müllen, T. Björnholm, *Chem. Eur. J.* **2001**, 7, 4894.

- [75] Z. Tomovic, M. D. Watson, K. Müllen, *Angew. Chem. Int. Ed.* **2004**, 43, 755.
- [76] V. Palermo, M. Palma, Z. Tomovic, M. D. Watson, R. Friedlein, K. Müllen, P. Samorì, *ChemPhysChem* **2005**, 6, 2371.
- [77] K. J. Kwak, S. Yoda, M. Fujihira, *Appl. Surf. Sci.* **2003**, 210, 73.
- [78] I. Lee, J. W. Lee, A. Stubna, E. Greenbaum, *J. Phys. Chem. B* **2000**, 104, 2439.
- [79] H. Sugimura, N. Saito, N. Maeda, I. Ikeda, Y. Ishida, K. Hayashi, L. Hong, O. Takai, *Nanotechnology* **2004**, 15, S69.
- [80] H. Sugimura, K. Hayashi, N. Saito, N. Nakagiri, O. Takai, *Appl. Surf. Sci.* **2002**, 188, 403.
- [81] B. Stiller, G. Knochenhauer, E. Markava, D. Gustina, I. Muzikante, P. Karageorgiev, L. Brehmer, *Mater. Sci. Eng., C* **1999**, 8–9, 385.
- [82] K. Umeda, K. Kobayashi, K. Ishida, S. Hotta, H. Yamada, K. Matsushige, *Jpn. J. Appl. Phys., Part 1* **2001**, 40, 4381.
- [83] H. Yamada, T. Fukuma, K. Umeda, K. Kobayashi, K. Matsushige, *Appl. Surf. Sci.* **2002**, 188, 391.
- [84] L. Bürgi, T. J. Richards, R. H. Friend, H. Sirringhaus, *J. Appl. Phys.* **2003**, 94, 6129.
- [85] L. Bürgi, R. H. Friend, H. Sirringhaus, *Appl. Phys. Lett.* **2003**, 82, 1482.
- [86] L. Bürgi, T. Richards, M. Chiesa, R. H. Friend, H. Sirringhaus, *Synth. Met.* **2004**, 146, 297.
- [87] K. Müller, A. Goryachko, Y. Burkov, C. Schwietz, M. Ratzke, J. Köble, J. Reif, D. Schmeisser, *Synth. Met.* **2004**, 146, 377.
- [88] T. Hassenkam, D. R. Greve, T. Björnholm, *Adv. Mater.* **2001**, 13, 631.
- [89] K. P. Puntambekar, P. V. Pesavento, C. D. Frisbie, *Appl. Phys. Lett.* **2003**, 83, 5539.
- [90] J. A. Nichols, D. J. Gundlach, T. N. Jackson, *Appl. Phys. Lett.* **2003**, 83, 2366.
- [91] T. Miyazaki, K. Kobayashi, K. Ishida, S. Hotta, T. Horiuchi, H. Yamada, K. Matsushige, *Jpn. J. Appl. Phys., Part 1* **2003**, 42, 4852.
- [92] H. Hoppe, T. Glatzel, M. Niggemann, A. Hinsch, M. C. Lux-Steiner, N. S. Sariciftci, *Nano Lett.* **2005**, 5, 269.
- [93] M. Chiesa, L. Bürgi, J.-S. Kim, R. Shikler, R. H. Friend, H. Sirringhaus, *Nano Lett.* **2005**, 5, 559.